UNIVERSITATEA BABEȘ-BOLYAI
BABEȘ-BOLYAI TUDOMÁNYEGYETEM
BABEȘ-BOLYAI UNIVERSITÄT
BABEȘ-BOLYAI UNIVERSITY
TRADITIO ET EXCELLENTIA

FACULTATEA DE FIZICĂ
Str. Mihail Kogălniceanu nr.1
Cluj-Napoca, RO-400084
Tel: +4(0)264-405300 | FAX: +4(0)264-591906
secretariat.phys@ubbcluj.ro
www.phys.ubbcluj.ro

UNIVERSITATEA "BABEȘ-BOLYAI" CLUJ-NAPOCA

FACULTATEA DE FIZICĂ

SPECIALIZAREA FIZICA CORPULUI SOLID

LUCRARE DE DISERTAȚIE

Coordonator științific
Lect. Dr. Ing. Sever Mican

Absolvent
Radu-George Hațegan

2022

UNIVERSITATEA BABEȘ-BOLYAI
BABEȘ-BOLYAI TUDOMÁNYEGYETEM
BABEȘ-BOLYAI UNIVERSITÄT
BABEȘ-BOLYAI UNIVERSITY
TRADITIO ET EXCELLENTIA

FACULTATEA DE FIZICĂ
Str. Mihail Kogălniceanu nr.1
Cluj-Napoca, RO-400084
Tel: +4(0)264-405300 | FAX: +4(0)264-591906
secretariat.phys@ubbcluj.ro
www.phys.ubbcluj.ro

UNIVERSITATEA "BABEȘ-BOLYAI" CLUJ-NAPOCA
FACULTATEA DE FIZICĂ
SPECIALIZAREA FIZICA CORPULUI SOLID

LUCRARE DE DISERTAȚIE

STRUCTURAL AND MAGNETIC PROPERTIES OF $DyFe_{2-x}Cu_x$ INTERMETALLIC COMPOUNDS

Coordonator științific
Lect. Dr. Ing. Sever Mican

Absolvent
Radu-George Hațegan

2022

Abstract

In this work, the structural and magnetic properties of intermetallic compounds of the $DyFe_{2-x}Cu_x$ are investigated through computational and experimental methods. The thesis is divided into four chapters. In the first chapter, a summary of the fundamental theory behind solid state physics, magnetism, magnetic materials and the magnetocaloric effect is provided. The second chapter is a review of the literature on the rare earth-transition metal intermetallic compounds, with an emphasis on the $DyFe_2$ compound. The third chapter briefly presents the main experimental and computational methods used for the characterization of the compounds. In the final chapter, the results are presented and discussed. Samples with the copper concentration ranging from $x = 0$ to $x = 1.5$ were prepared by arc melting under an inert Ar atmosphere followed by annealing at 950 °C for 4 days. The samples were characterized by X-ray diffraction (XRD) and it was found that for copper concentrations $x > 0.5$ they presented a mixture of phases between $DyFe_2$ and $DyFe_3$. The magnetic measurements that were performed were magnetization and susceptibility measurements through the vibrating sample magnetometer (VSM) and a Faraday-Weiss balance. Electronic structure calculations were performed using Abinit software package, with the projector augmented wave method (PAW), in the generalized gradient approximation (GGA). Both the experimental and computational results showed that the addition of copper does not significantly affect the lattice parameters, an expected result, given the similar atomic radii of Fe and Cu. Also, the lattice parameters determined from the electronic structure calculations were in good agreement with the experimentally determined ones. The magnetic moments were determined computationally and it has been found that the total magnetic moment of the compounds increases with the copper concentration, as expected, although the Dy atomic magnetic moments are underestimated due to the fact that the computational method does not account for the spin-orbit coupling. From the Weiss balance measurements, the Curie temperature has been determined and it has been found that it decreases with increasing copper concentration. The VSM measurements showed that the coercive field increases with the copper concentration, while the saturation magnetization decreases. This behaviour could be attributed to the effect of copper on the crystalline field and the enhancement of the magnetocrystalline anisotropy. These properties may be of interest in fields related to magnetic materials, such as spintronics.

Contents

Introduction 4
1. Fundamental theory of Solid State Physics and Magnetism 5
1.1. Solid State Physics 5
1.2. Electronic structure 8
1.3. Magnetism and magnetic materials 10
1.4. The magnetocaloric effect 14
2. Rare Earth – Transition Metal Intermetallic Compounds 17
2.1. General aspects 17
2.2. Physical properties 19
2.3. The $DyFe_2$ intermetallic compound 21
3. Experimental and computational methods 24
3.1. Arc melting 24
3.2. X-Ray Diffraction 25
3.3. Vibrating sample magnetometry 26
3.4. The Weiss balance 28
3.5. Computational methods 29
4. Results and discussions 36
Conclusions 49
References 50

Introduction

The purpose of this study is the structural and magnetic characterization of the $DyFe_{2-x}Cu_x$ intermetallic compounds and the effect of copper doping on the magnetic properties, which may lead to potential applications for these materials, such as active materials in magnetic refrigerators or as magnetic substrates in spintronic devices. The study was performed both computationally, using the PAW-GGA+U method and the Abinit software package, as well as experimentally. The samples were prepared by arc-melting followed by annealing. The structural properties were investigated by means of X-ray diffraction, while the magnetic properties were investigated using the vibrating sample magnetometer and the Faraday-Weiss balance.

The thesis consists of four chapters. In the first chapter, the fundamental theory regarding condensed matter and magnetism is summarized. The crystallographic structure and the theory and models that allow the structural characterization of crystalline materials are emphasized. The fundamentals of magnetism and magnetic material types are then presented and the magnetocaloric effect is also briefly discussed, since it is of interest in the developing field of magnetic refrigeration.

The second chapter provides a scientific literature study on the rare earth – transition metal intermetallic compounds, their structural and magnetic properties, with an emphasis on the magnetocaloric effect for which this class of materials proved to have some applications. The physical properties of $DyFe_2$ are of particular interest.

The third chapter describes the main experimental and computational methods used for the elaboration and characterization of the compounds. Arc melting, a common method for elaborating intermetallic samples is presented. XRD, the main structural characterization method is discussed. The vibrating sample magnetometer (VSM) and Faraday-Weiss balance as means to determine the main magnetic properties of materials are briefly described. The computational methods that are presented are density functional theory (DFT), the projector augmented wave method (PAW), the generalized gradient approximation (GGA) and pseudopotentials.

In the fourth and final chapter, the results of the computational and experimental characterizations are presented. The main details regarding the computational parameters, the sample preparation and experimental measurements are provided. The results of the electronic structure DFT calculations are compared to the experimentally determined ones and the behaviour of the magnetic properties with respect to copper doping are discussed. The four chapters are followed by conclusions and references.

1. Fundamental theory of Solid State Physics and Magnetism

1.1. Solid State Physics

A crystal can be obtained by adding atoms in a solution [1]. As atoms or groups of atoms are added, a three-dimensional periodic array of identical building blocks is formed [1]. The ideal crystal results from the infinite repetition of identical groups of atoms called the basis [1]. The lattice is the set of mathematical points to which the basis is attached [1]. It can be defined by three translation vectors a_1, a_2 and a_3 so that crystal looks the same when viewed from the point r as when viewed from every point r' translated by an integral multiple of the a's:

$$r' = r + u_1 a_1 + u_2 a_2 + u_3 a_3 \tag{1.1}$$

where u_1, u_2 and u_3 are arbitrary integers [1].

The lattice is a primitive lattice if (1.1) is always satisfied for two points from which the spatial configuration of the atoms looks the same [2]. Therefore, a_1, a_2 and a_3 are in this case primitive vectors [1]. A crystal is formed by adding a basis to each lattice point - figure 1.1 [1]. The position of a basis atom i relative to the lattice point can be expressed as a linear combination of the primitive vectors [1]:

$$r_i = x_i a_1 + y_i a_2 + z_i a_3 \tag{1.2}$$

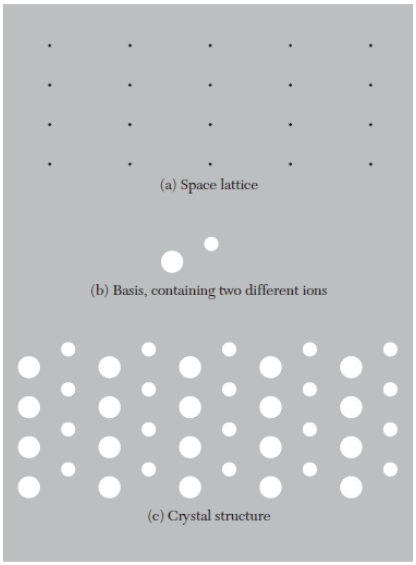

Figure 1.1. Formation of the crystal structure [1].

A unit cell is a cell that can generate the entire crystal by repeated translation operations [2]. The primitive cell is the minimum-volume unit cell – figures 1.2, 1.3 [1]. It is a parallelepiped defined by the primitive vectors, with the volume equal to:

$$V = |a_1 \cdot a_2 \times a_3| \tag{1.3}$$

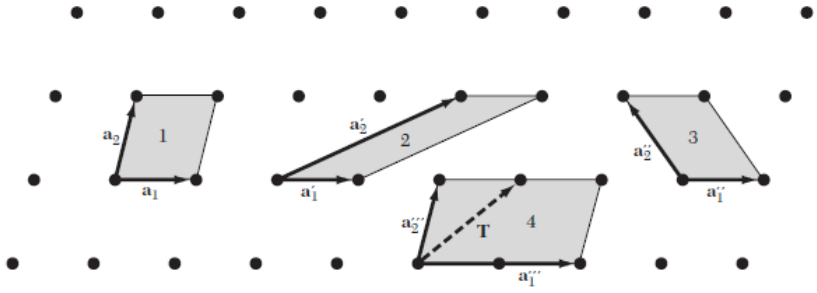

Figure 1.2. Lattice in 2D. Parallelograms 1, 2 and 3 are primitive cells, while 4 is not. [1].

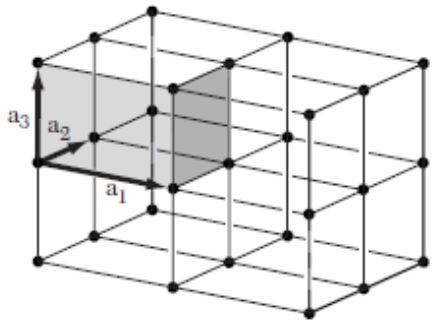

Figure 1.3. Lattice in 3D [1].

There are 14 three-dimensional lattice types, presented in table 1.1 [1]. The angles between the a_1, a_2 and a_3 axes are denoted by α, β and γ. The lattices in the cubic system are the simple cubic (SC) lattice, the body-centered cubic (BCC) lattice, and the face-centered cubic (FCC) lattice - figure 1.4 [1].

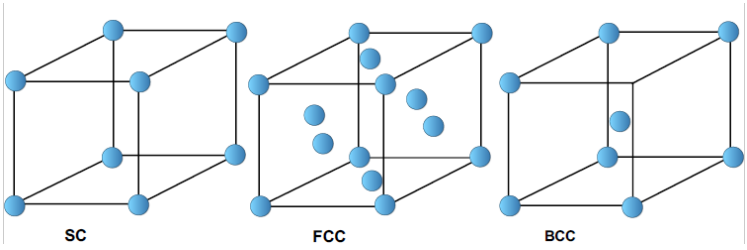

Figure 1.4. Cubic system lattice types.

Table 1.1. 3D lattice types.

System	No. Lattices	Relation between cell axes and angles
Triclinic	1	$a_1 \neq \alpha_2 \neq \alpha_3$, $\alpha \neq \beta \neq \gamma$
Monoclinic	2	$a_1 \neq \alpha_2 \neq \alpha_3$, $\alpha = \beta = 90° \neq \gamma$
Orthorhombic	4	$a_1 \neq \alpha_2 \neq \alpha_3$, $\alpha = \beta = \gamma = 90°$
Tetragonal	2	$a_1 = \alpha_2 \neq \alpha_3$, $\alpha = \beta = \gamma = 90°$
Cubic	3	$a_1 = \alpha_2 = \alpha_3$, $\alpha = \beta = \gamma = 90°$
Trigonal	1	$a_1 = \alpha_2 = \alpha_3$, $\alpha = \beta = \gamma < 120°, \neq 90°$
Hexagonal	1	$a_1 = \alpha_2 \neq \alpha_3$, $\alpha = \beta = 90°$ $\gamma = 120°$

A crystal plane's orientation is given by three points in that plane, called Miller indices [2]. These are determined by finding the intercepts on the axes in terms of the lattice constants a_1, a_2 and a_3, taking their reciprocals and finding the smallest three integers that have the same ratio [1]. The result is usually denoted by (hkl), where h, k and l are the Miller indices corresponding to that given plane [1].

Crystal structure can be studied through photon, neutron or electron diffraction, by making use of Bragg's Law (1.4) [3].

$$2d \sin\theta = n\lambda \tag{1.4}$$

In equation 1.4, d is the interplanar spacing (distance between parallel lattice planes), λ is the wavelength of the incident radiation and θ is the angle of incidence (between the incident wave and the atomic plane) [3].

The incident radiation must have a suitable wavelength, since the Bragg law only stands for $\lambda \leq 2d$ [3].

To determine the crystal structure from diffraction patterns, a Fourier analysis of the lattice proves to be useful. A crystal has a spatial periodicity due to it being invariant to translations of

the form $T = u_1a_1 + u_2a_2 + u_3a_3$, so the electron number density also has the same periodicity [1]. This allows the following mathematical relation:

$$n(r + T) = n(r) \tag{1.5}$$

where $n(r)$ is the electron density at the lattice point described by the position vector r [1].

The relation in 1.5 allows the Fourier expansion of the electron density in the following way:

$$n(r) = \sum_G n_G \exp(iG \cdot r) \tag{1.6}$$

where G is a set of vectors such that $n(r)$ is invariant under any translations of type T [1].

The Fourier representation of the crystal lattice is called the reciprocal lattice and it is mapped by the vectors G from 1.6. The points in the reciprocal lattice are described by:

$$G = v_1b_1 + v_2b_2 + v_3b_3 \tag{1.7}$$

where v_1, v_2 and v_3 are integers and b_1, b_2 and b_3 are the reciprocal lattice primitive vectors [1]. The reciprocal lattice primitive vectors are related to the real lattice primitive vectors by:

$$b_i \cdot a_j = 2\pi\delta_{ij} \tag{1.8}$$

where δ_{ij} is the Kronecker delta function [1].

The intensity of the scattered waves is proportional to the square of the structure factor, given by:

$$F_G = \sum_f f_j \exp(-iG \cdot r_j) \tag{1.9}$$

where f_j is the atomic form factor, which is an atom specific constant [1]. For a given crystallographic plane, described by the Miller indices h, k and l, the structure factor can be therefore expressed as [1]:

$$F(hkl) = \sum_{j=1}^{n} f_j \exp[2\pi i(hx + ky + lz)] \tag{1.10}$$

From formula 1.10, the lattice parameters a_1, a_2 and a_3 for the different crystallographic structures can be determined from the diffraction pattern, using Bragg's law.

1.2. Electronic structure

An accurate model describing the electronic structure of solids is the energy band model, based on the nearly free electron model. In this approximation, the conduction electrons in the solid are subjected to a weak periodic potential due to their interaction with the ion cores in the lattice. Hence, they are called "nearly free". According to Bloch's theorem, if the electrons are in a periodic potential, their wavefunctions can be expressed as:

$$\psi_k(r) = u_k(r) \exp(ik \cdot r) \tag{1.11}$$

where $u_k(r)$ is a function with the same periodicity as the crystal lattice [1].

In the Kronig-Penney model, the lattice potential is assumed to be a square-well periodic potential, such as the one from figure 1.5 [1].

The band structure formation can be explained by this model [4]. The appearance of band gaps is the consequence of the Bragg reflection of electrons, where there are no wave solutions for the Schrödinger equation - figure 1.6 [1].

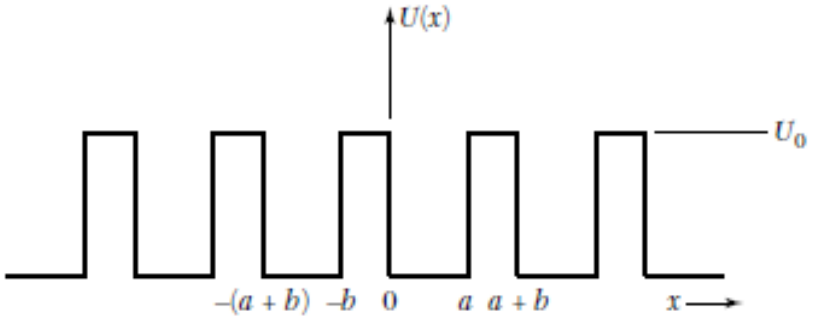

Figure 1.5. Kronig-Penney square well potential [1].

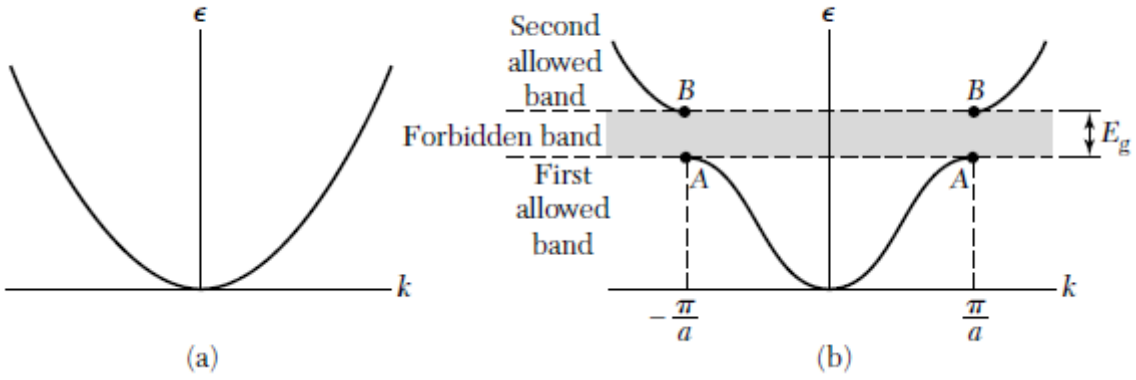

Figure 1.6. Energy as a function of the wavevector for the: (a) free electron model and (b) nearly-free electron model [1].

The Bragg diffraction condition in one dimension is:

$$k = \pm\frac{1}{2}G = \pm n\frac{\pi}{a} \tag{1.12}$$

The first reflections take place in the k space at $\pm\frac{\pi}{a}$ [1]. The region between these values is called the first Brillouin zone [1]. The Fermi energy is the energy of the topmost filled electron level in the ground state of a multiple electron system [1].

The nearly free electron model can qualitatively describe the electrical nature of a crystal [4]. If the valence electrons completely fill one or more bands and leave the other empty, the crystal

is an insulator or semiconductor (depending on the magnitude of the band gap), whilst if the bands overlap (or are partly filled) it is a metal or semimetal - figure 1.7 [1].

An important quantity related to the electronic structure of solids, which determines a wide range of physical properties is the electronic density of states, which describes the number of occupied states in a system at a given energy [4]. This quantity is of particular interest in ab-initio density functional theory (DFT) type of calculations, through which the structure and some properties of the solid can be determined [4].

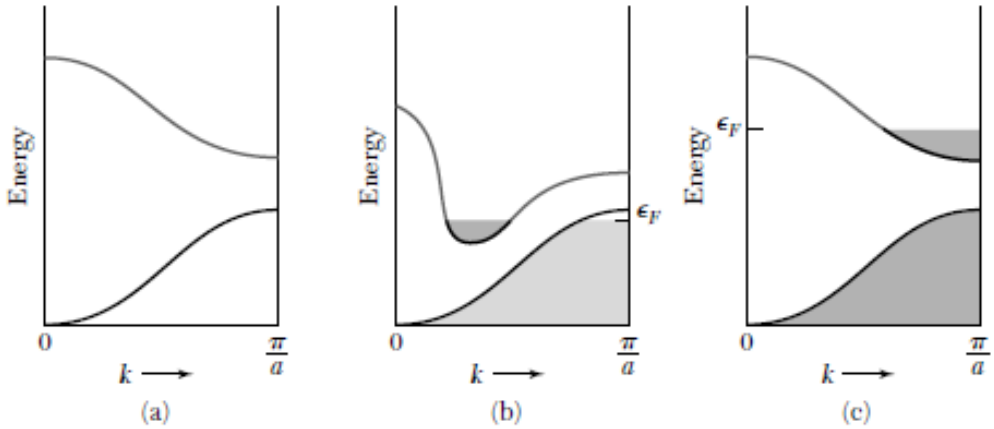

Figure 1.7. (a) is an insulator or semiconductor, (b) and (c) are metals [1].

1.3. Magnetism and magnetic materials

Although the classical Maxwell equations provided a physical explanation for a wide range of macroscopic phenomena, it wasn't until the discovery of the electron spin in 1925, when it became clear that the magnetic properties of a material are related to this quantity and therefore, to its electronic structure [5]. Werner Heisenberg provided a quantum mechanical microscopic model of magnetism through the Heisenberg Hamiltonian, which describes the interaction between two neighbouring atoms with spins S_i and S_j:

$$\mathcal{H} = -2JS_i \cdot S_j \tag{1.13}$$

where J is the exchange constant [5]. The sign of this constant is related to the magnetic ordering of the system, being positive for ferromagnetic materials and negative for antiferromagnetic or ferrimagnetic materials [5].

The elementary quantity in magnetism is the magnetic moment m. On an atomic level, this can be described by:

$$m = g\mu_B\sqrt{J(J+1)} \tag{1.14}$$

where g is the Landé factor, μ_B the Bohr magneton and J the total angular momentum [5].

The magnetization M in a mesoscopic volume δV can be defined as the volume average of the magnetic moments [5]:

$$M = \frac{\delta m}{\delta V} \tag{1.15}$$

The concept can be extended to a macroscopic sample:

$$M = \frac{\sum_i M_i V_i}{\sum_i V_i} \tag{1.16}$$

where i indicates a domain with an M_i magnetization and V_i volume [5].

The primary magnetic field (magnetic induction) B associated to a material is related to the applied field H and magnetization M by:

$$B = \mu_0(H + M) \tag{1.17}$$

where μ_0 is the magnetic permeability of vacuum [5].

The different types of magnetic materials can be explained through a quantity called susceptibility which relates the magnetization to the H field [6]:

$$\chi = \frac{M}{H} \tag{1.18}$$

The susceptibility describes the behaviour of materials under an applied magnetic field and based on it, materials can be classified in the following categories [6]:

i) Diamagnetic: the susceptibility is negative and therefore, the applied fields are expelled from the material. The magnetic moments of the atoms are null.

ii) Paramagnetic: the spins are not null, but randomly oriented, therefore the total magnetic moment is zero. The susceptibility is positive, but very small, therefore, if the applied field is large enough, the spins will align in its direction.

iii) Ferromagnetic: the spins are aligned in the same direction (parallel). The susceptibility is positive and larger than in paramagnetic materials, therefore the material is easier to magnetize.

iv) Antiferromagnetic: the spins are arranged in anti-parallel sublattices which will determine a zero total magnetic moment.

v) Ferrimagnetic: the spins are anti-parallel, but they have different magnitudes, so the total magnetic moment will be non-zero.

Depending on the type of magnetic order, the susceptibility has a temperature variation described by different variation laws.

In the case of paramagnetic materials, this is the Curie law [6]:

$$\chi = \frac{C}{T} \tag{1.19}$$

C is the Curie constant given by:

$$C = \frac{N\mu_0\mu_B^2 g^2 J(J+1)}{3k_B} \tag{1.20}$$

where, N is the number of atoms per unit volume [6].

In ferromagnetic materials, which present a spontaneous magnetization and have a net moment different than zero even in the absence of an applied field, the susceptibility obeys the Curie-Weiss law:

$$\chi = \frac{C}{T-\Theta} \tag{1.21}$$

where Θ is a critical temperature called the Curie temperature (T_C), above which, the system will lose its magnetic ordering and become paramagnetic [6].

Antiferromagnetic materials also present a critical temperature, called Néel tempetarure (T_N). At temperatures above the Néel tempetarure, the system loses its antiferromagnetic ordering and becomes paramagnetic. In this region, the susceptibility has a temperature variation similar to that of ferromagnets [6]:

$$\chi = \frac{C}{T+\Theta} \tag{1.22}$$

In ferrimagnetic materials, the susceptibility obeys a Néel hyperbolic law [6]:

$$\frac{1}{\chi} = \frac{1}{\chi_0} + \frac{T}{C} - \frac{\sigma}{T-\theta} \tag{1.23}$$

The susceptibility of diamagnetic materials was determined by Landau in the free electron model as:

$$\chi = -\frac{n\mu_0\mu_B^2}{2k_B T_F} \tag{1.24}$$

where n is the electron density and T_F the Fermi temperature (temperature corresponding to the Fermi energy) [5].

The first succesful description of ferromagnetic behaviour was the molecular field theory, developed by Pierre Weiss in 1906, which is a mean field theory, based on the assumption that in ferromagnets, there is an internal 'molecular field', which is an average magnetic field, proportional to the magnetization:

$$H^i = n_w M + H \tag{1.26}$$

where n_w is a proportionality coefficient called the Weiss coefficient [5].

This assumption led to the following magnetization law:

$$M = M_0 B_J(x) \tag{1.27}$$

where M_0 is the zero-field magnetization, B_J is the Brillouin function and x is given by [5]:

$$x = \mu_0 m_0 (n_w M + H)/k_B T \tag{1.28}$$

The theory is in good agreement with the experimentally observed ferromagnetic behavior - figure 1.8 [5]. In the small x limit, the Curie-Weiss law is obtained above T_c. The Curie temperature is also determined as:

$$T_C = n_w C \tag{1.29}$$

where C is the Curie constant [5].

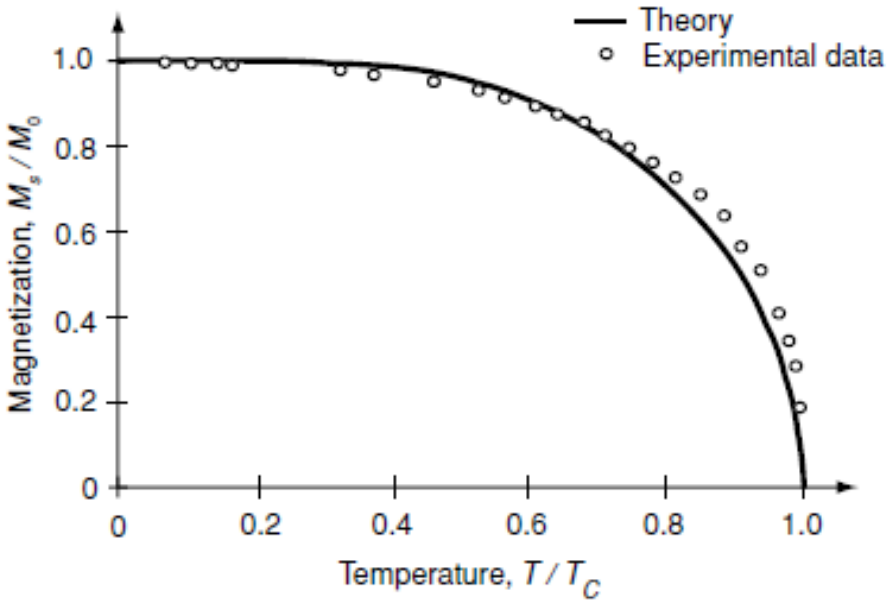

Figure 1.8. The spontaneous magnetization for nickel and the theoretically predicted one [5].

The different susceptibility laws for different types of magnetic materials are plotted in figure 1.9 [7].

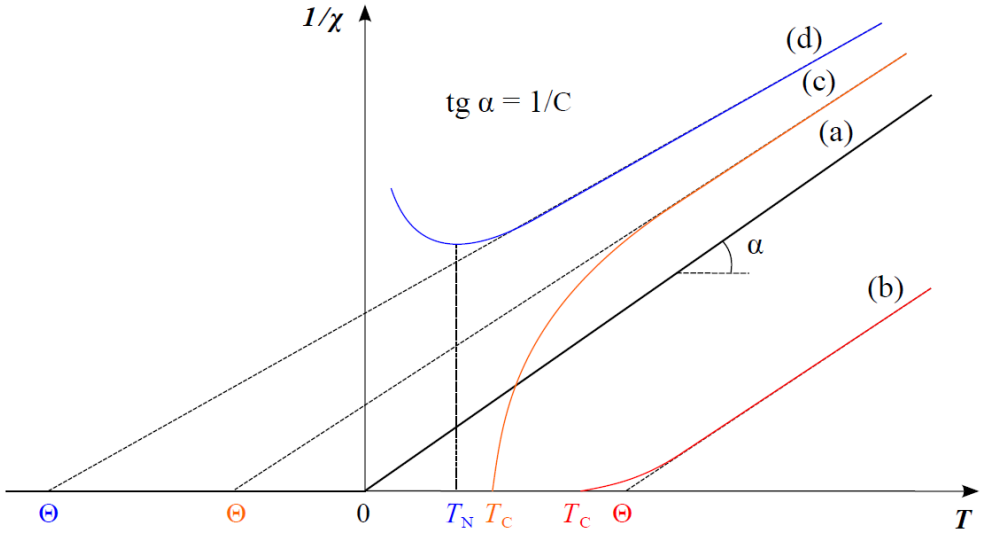

Figure 1.9. The inverse of susceptibility as a function of temperature for: (a) paramagnets, (b) ferromagnets, (c) ferrimagnets and (d) antiferromagnets [7].

1.4. The magnetocaloric effect

An important consequence of the discovery of the electron spin and magnetic properties of materials is the growing interest in potential applications related to these properties. A wide range of applications are related to the magnetocaloric effect.

The magnetocaloric effect manifests as a change in a material's temperature under adiabatic magnetization [8]. The growing interest in the study of this effect in different materials is due to the potential replacement of conventional vapour-gas cycle refrigerators with magnetic refrigerators [8].

Magnetic refrigeration is a process in which a magnetic material is subjected to a magnetic field. When the field is applied, the material is magnetized and will increase its temperature. The material is kept in this magnetized state until it radiates its heat. When removing the applied field, the material is demagnetized and cools below the initial temperature.

The thermodynamical description of the effect is based on the expression of the total differential of the internal energy U, in terms of the entropy S, the volume V and a magnetic energy term depending on the magnetization M and an applied field H [8]:

$$dU = TdS - pdV - MdH \tag{1.30}$$

By making use of the known thermodynamical potentials and typical variational calculus, the magnetocaloric effect can be described by the following equation:

$$\Delta \mathrm{T_{ad}} = -\int_{\mathrm{H_0}}^{\mathrm{H_1}} \left(\frac{\mathrm{T}}{\mathrm{C(T,H)}}\right)_H \left(\frac{\partial \mathrm{M(T,H)}}{\partial \mathrm{T}}\right)_H \mathrm{dH} \tag{1.31}$$

where $\Delta \mathrm{T_{ad}}$ is the adiabatic temperature variation and C is the heat capacity of the material [8].

The change in entropy corresponding to the adiabatic temperature change is [8]:

$$\Delta \mathrm{S(T)} = \int_{\mathrm{H_1}}^{\mathrm{H_0}} \left(\frac{\partial \mathrm{M(T,H)}}{\partial \mathrm{T}}\right) \mathrm{dH} \tag{1.32}$$

Through further simplification, one can obtain the following equation:

$$\Delta T = -\frac{T\Delta S}{C_H} \tag{1.33}$$

where C_H is the heat capacity [8].

Taking into account the Curie and Cuire-Weiss laws, the entropy change can be expressed for a paramagnet (1.34) and ferromagnet above room temperature (1.35):

$$\Delta \mathrm{S} = -\frac{1}{2}\frac{C_J \Delta(H)^2}{T^2} \tag{1.34}$$

$$\Delta \mathrm{S} = -\frac{1}{2}\frac{C_J \Delta(H)^2}{(T-T_C)^2} \tag{1.35}$$

where C_J is the Curie constant [8].

From these equation, it is trivial to conclude that the magnitude of the magnetocaloric effect reaches a maximum at the transition (Curie) temperature, where both the entropy change and temperature variation are the highest. It is also obvious that the effect increases with increasing applied fields. These results were confirmed experimentally in various compounds through heat capacity measurements, such as pollycrystalline GdPd - figure 1.10 and polycrystalline Dy - figure 1.11 [8].

An important parameter that describes the efficiency of a magnetic material for refrigeration purposes is the relative cooling power (RCP) defined as:

$$RCP = \Delta S^{max} \Delta T_{FWHM} \tag{1.36}$$

where ΔS^{max} is the maximum magnetic entropy variation and ΔT_{FWHM} is the full width at half maximum of the magnetic entropy curve [9].

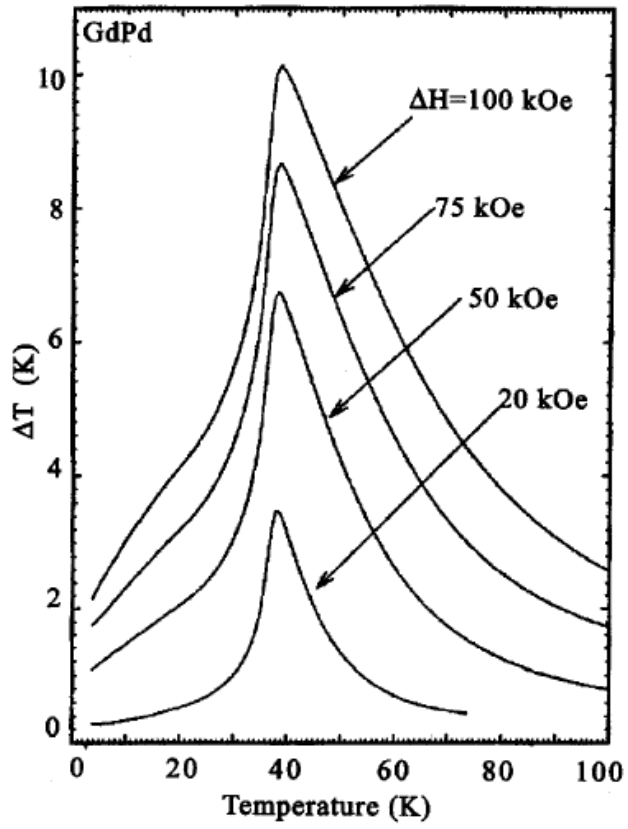

Figure 1.10. Magnetocaloric effect in polycrystalline GdPd [8].

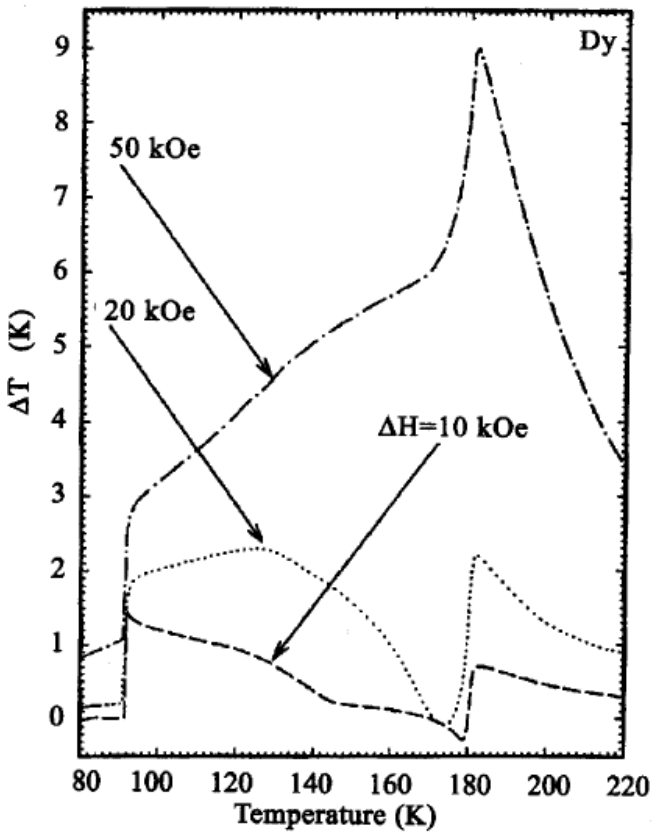

Figure 1.11. Magnetocaloric effect in polycrystalline Dy [8].

The current challenge in material science regarding magnetic refrigeration is the synthesis of materials with high RCP and a Curie temperature close to room temperature, since this would allow commercial applications, such as room temperature refrigeration.

2. Rare Earth – Transition Metal Intermetallic Compounds

2.1. General aspects

Intermetallic compounds are alloys of two or more metals with well defined stoichiometric compositions [10]. The distinction between intermetallic compounds and solid solutions is that in the case of intermetallic compounds, the atoms are not randomly distributed, but have definite positions in the crystallographic unit cell, the position being different for each of the different atoms [10]. It has been found that the intermetallic compound does not necessarily have similar physical properties to the composing elements [10]. Therefore, there is a high interest in investigating such kind of compounds for potential applications [10].

The condition for the formation of an intermetallic compound in a binary system of metals A and B is that the heat of formation ΔH of the compound is negative [10].

In table 2.1, the heats of formation for different rare earth – transition metal (R-M) intermetallic compounds are presented [10].

Table 2.1. Heat of formation (kJ/g) for different R-M compounds [10].

M	YM_5	YM_2	YM	Y_3M	ScM	LaM	EuM	ThM
Sc	+1	+1	+1	+1	—	+11	+8	−0
Ti	+9	+17	+17	+14	+8	+38	+14	+9
V	+14	+24	+24	+20	+10	+50	+15	+12
Cr	+9	+16	+15	+13	+1	+43	+13	+3
Mn	−1	−2	−2	−2	−12	+19	+7	−11
Fe	−1	−2	−2	−1	−17	+28	+9	−15
Co	−18	−30	−30	−26	−42	−3	+1	−41
Ni	−26	−44	−43	−37	−55	−17	−2	−54

For a given R component, the stability of the compounds increases in the direction of Mn, Fe, Co and Ni [10]. For a given metal M, the stability increases in the La to Lu direction [10].

The majority of R-M intermetallic compounds crystal structures are related and originate from the $CaCu_5$ hexagonal lattice type - figure 2.1 [10].

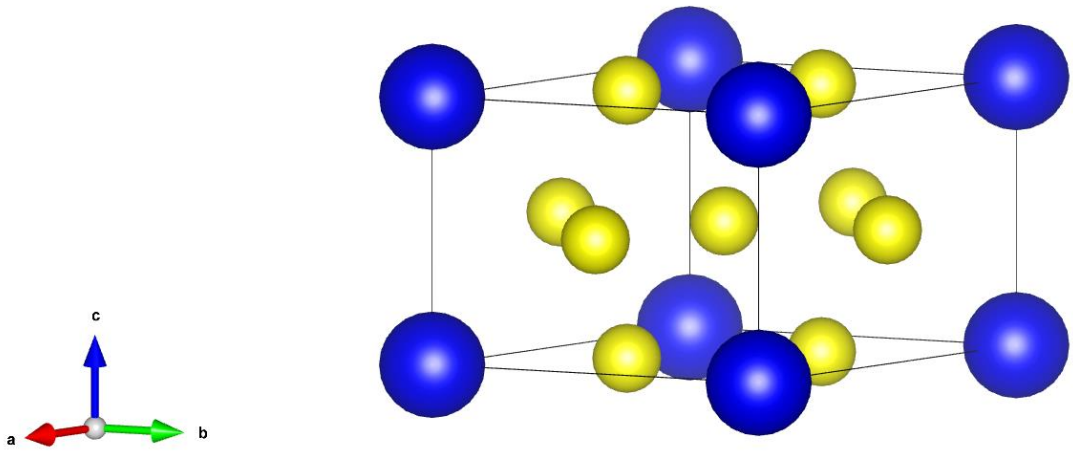

Figure 2.1. Unit cell of the $CaCu_5$ structure. The Ca atoms are depicted in blue, while the Cu atoms are yellow [11].

Depending on the stacking arrangement of these unit cells, different R-M compounds can be formed - figure 2.2 [10].

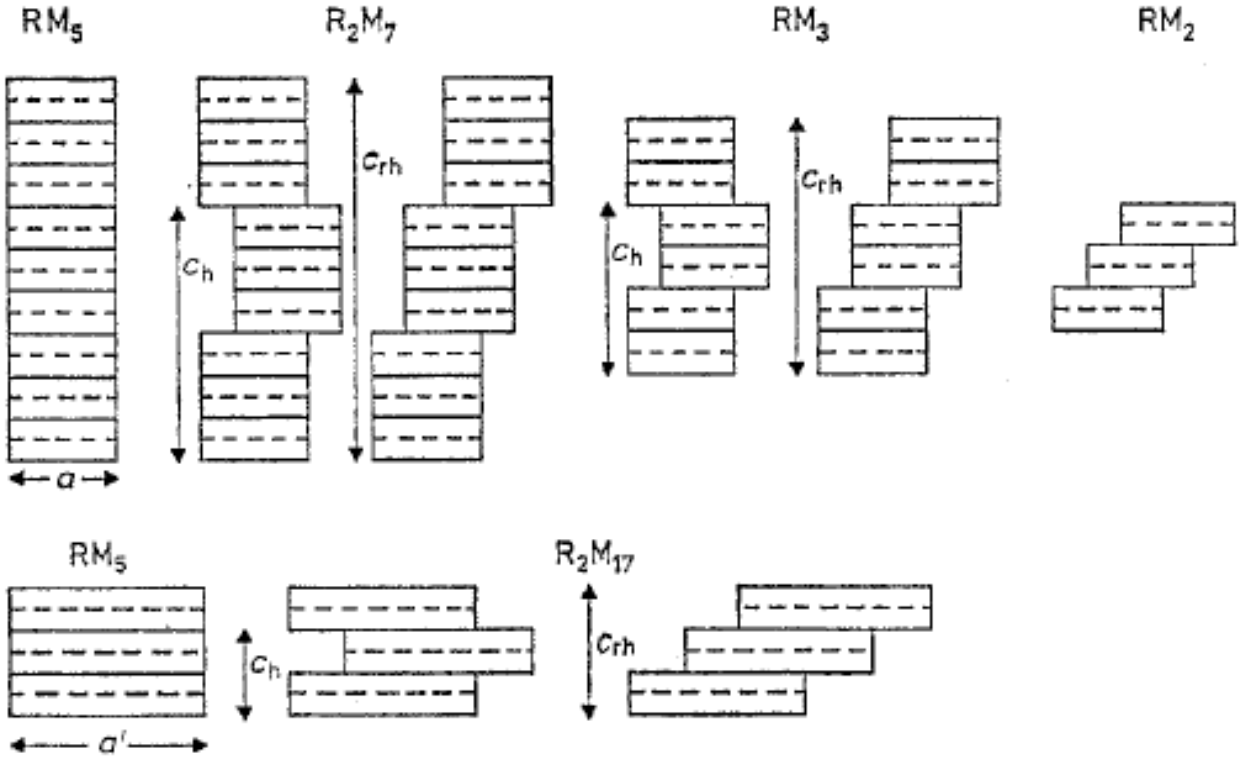

Figure 2.2. Stacking of different R-M compounds [10].

Some common R-M structures are presented in table 2.2 [10]. RM_2 compounds crystallize in the $MgCu_2$ type cubic structures or $MgZn_2$ hexagonal structures. These are obtained by replacing the M atoms by R atoms in RM_5 structures [10].

Table 2.1.2. Different R-M compounds structure types [10].

Compound	Lattice symmetry	Structure type	M
R_3M	Orthorhombic	Al_3Ni	Ni, Co
R_7M_3	Hexagonal	Th_7Fe_3	Ni
R_4M_3	Hexagonal	Ho_4Co_3	Co
RM	Orthorhombic	FeB or CrB	Ni
RM_2	Cubic	$MgCu_2$	Ni, Co, Fe, Mn
RM_2	Hexagonal	$MgZn_2$	Mn
RM_3	Hexagonal	$CeNi_3$	Ni
	Rhombohedral	$PuNi_3$	Ni, Co, Fe
R_2M_7	Hexagonal	Ce_2Ni_7	Ni, Co
	Rhombohedral	Gd_2Co_7	Ni, Co
R_6M_{23}	Cubic	Th_6Mn_{23}	Fe, Mn
RM_5	Hexagonal	$CaCu_5$	Ni, Co
R_2M_{17}	Hexagonal	Th_2Ni_{17}	Ni, Co, Fe
	Rhombohedral	Th_2Zn_{17}	Co, Fe
RMn_{12}	Tetragonal	$ThMn_{12}$	Mn

2.2. Physical properties

For R-Ni compounds there is a low interest with regard to magnetic properties, due to the magnetic ordering temperature being much lower than room temperature, with Gd_2Ni_{17} having a higher value at around 200K [10]. The highest ordering temperatures are found in R-Co compounds (up to 1290K in $LaCo_{13}$) [10]. For Fe compounds, the temperatures lie between the ones for the Ni and Co compounds and it has been noted that in R-Fe compounds the highest ordering temperatures are observed for the compositions with a lower concentration of Fe (such as $GdFe_2$, with a T_c=796K) [10].

For $DyFe_2$ and $ErFe_2$ single crystals, Clark and Belson (1973) found that the saturation magnetization was 10% higher than for the polycrystalline materials.

The magnetic interactions in R-M compounds are of three main types: R-R interaction, M-M interactions and R-M interactions.

The R-R interaction is the weakest and it is indirect since there is no overlap of the 4f wavefunctions [10]. A possible interaction channel is through the spin polarization of the s-conduction electrons [10]. This interaction has a damped oscillatory nature and it is of the RKKY (Ruderman–Kittel–Kasuya–Yosida) type [10].

The M-M interaction is the strongest one due to the spatial extent of the 3d wavefunctions being much larger than that of 4f electrons which leads to a strong overlap between wavefunctions of neighbouring atoms and the formation of 3d energy bands instead of 3d levels [10]. The strong exchange interaction between 3d electrons can lead to the number of spin-up and spin-down electrons not being equal - figure 2.3 [10].

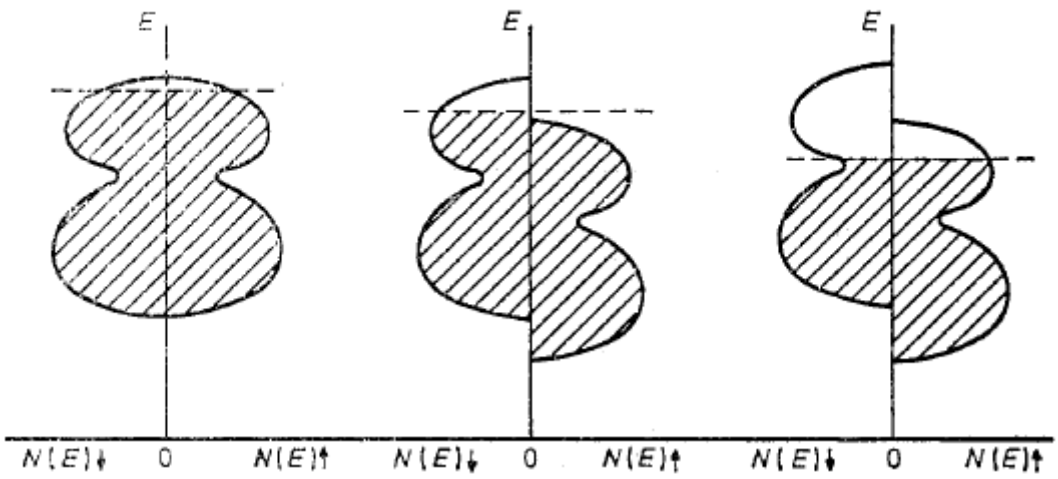

Figure 2.3. Energy as a function of density of states for spin-up N(E)↑ and spin-down N(E)↓ electrons in the three possible cases. The Fermi energy is represented by the broken lines [10].

The existence of a net magnetic moment is predicted in the Stoner model through the Stoner criterion:

$$IN(E_F) > 1 \tag{2.1}$$

where I is the effective Coulomb repulsion between 3d electrons and $N(E_F)$ is the 3d electron density of states at the Fermi level [10].

In the Stoner-Wohlfarth model, the Curie temperature is given by:

$$T_C^2 = T_F^2(IN(E_F) - 1) \tag{2.2}$$

where T_F is the degeneracy temperature and it depends on the first and second derivatives of $N(E)$ at the paramagnetic Fermi level [10]. It should be noted, however, that this description is an oversimplification, only valid for weak itinerant ferromagnets and can at best show general trends [10].

The R-M magnetic interaction strength is between those of R-R and M-M [10]. If both R and M carry a magnetic moment, there is an antiparallel coupling between the R and M sublattices if R is a heavy rare-earth element and parallel if R is a light rare-earth element [10]. This behaviour is explained through the assumption that the 3d moments couple antiferromagnetically with the spin moment of the rare-earth [10]. The observed difference between light and heavy rare-earth elements comes from the fact that in light R compounds, the total rare-earth angular momentum is J=L-S and in heavy R compounds, it is J=L+S [10].

In RFe_2 Burzo found that the 3d moments μ_M are scaled linearly with the exchange field acting on them $H_{ex}(M)$ through a proportionality constant V_M:

$$\mu_M = \mu_M(0) + V_M H_{ex}(M) \tag{2.3}$$

where $\mu_M(0) = 1.44\mu_B$ for RFe_2 compounds [10].

2.3. The $DyFe_2$ intermetallic compound

Experimental data from the literature showed that $DyFe_2$ crystallizes in a C15 (FCC, space group 227) $MgCu_2$ type face-centered cubic structure - figure 2.4 [12]. There are several reported values for the lattice parameters, such as 7.324 Å [13] and 7.285 Å [12].

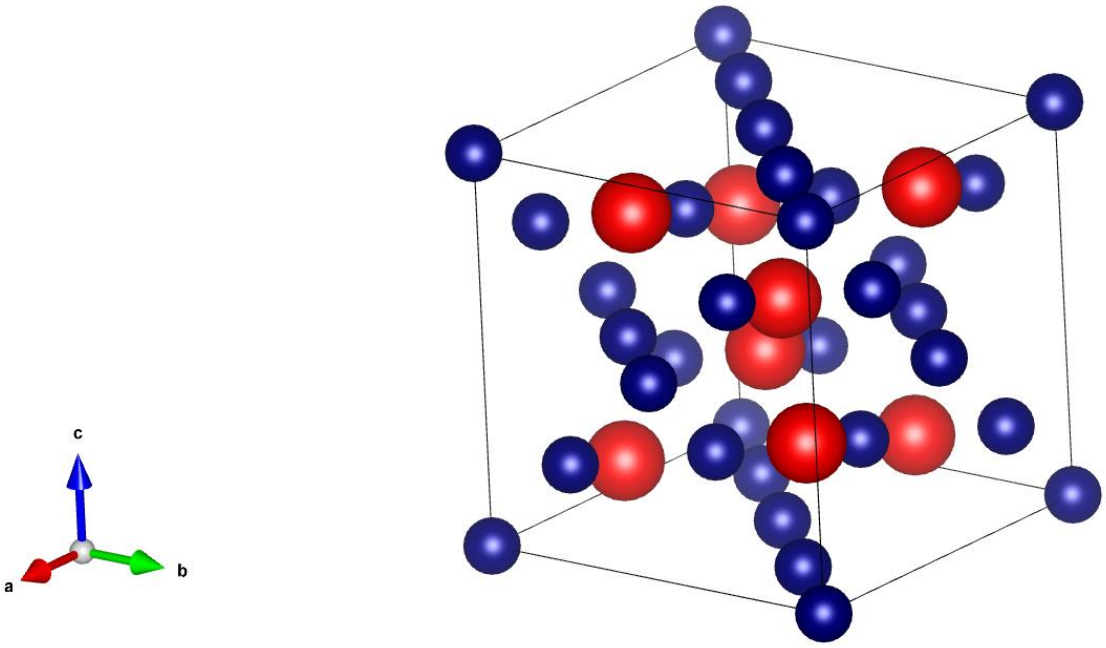

Figure 2.4. $DyFe_2$ unit cell with Fe atoms in blue and Dy atoms in red [11].

The experimental phase diagram shows that the $DyFe_2$ intermetallic compound is formed at the 66.6% Fe and 33.3% Dy weight fraction in a peritectic reaction at 1270 ℃ - figure 2.5 [14].

The Curie temperature of 638 K was experimentally determined by Mansmann and Wallace (1964) [12]. The reported values for the saturation magnetization are 4.91 μ_B at 4.2 K, 4.97 μ_B at 77 K and 3.19 μ_B at 300K [12]. The magnetization-temperature curve from figure 2.6 suggests that $DyFe_2$ and $GdFe_2$ are ferrimagnetic materials, since they do not follow a Brillouin function, but decrease rather linearly with the temperature throughout most of the temperature range [12]. Bleaney showed that the Co moment in $LnCo_2$ compounds is proportional to $(g-1)M_e/g$, where g is the Landé factor and M_e the effective moment of the lanthanide [12]. Assuming this model, the Fe moment of 1.68 μ_B is estimated for the $DyFe_2$ compound [12]. The reason for the reduction of the Fe magnetic moment in the compound in comparison to elemental Fe is electron transfer from the lanthanide to the Fe atoms [12].

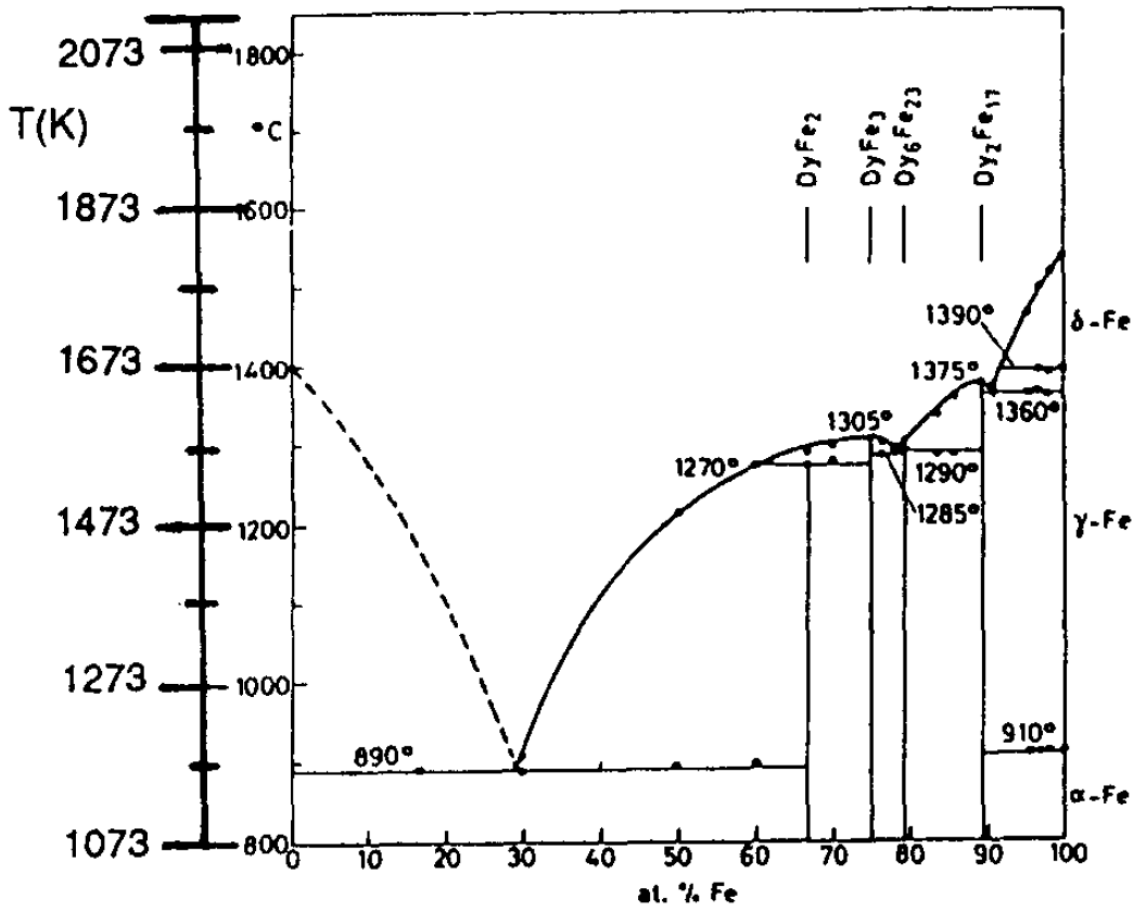

Figure 2.5. Fe-Dy phase diagram by Buschow and van der Goot [14].

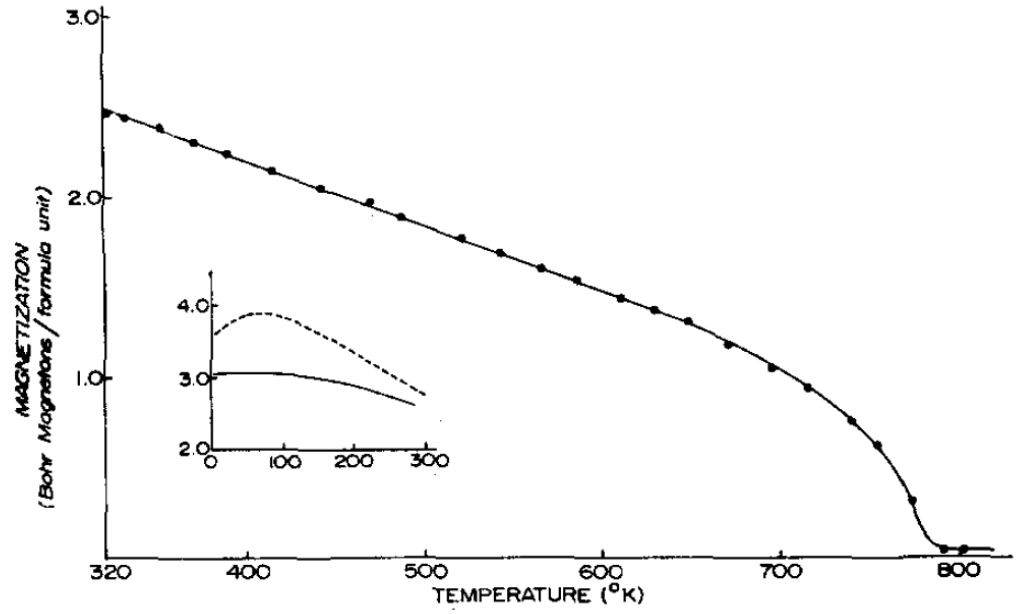

Figure 2.6. Magnetization as a function of temperature for $GdFe_2$ and $DyFe_2$ (dotted curve) at 2.2kOe [12].

Similar results were reported by A. E. Clark, R. Abbundi and W. R. Gillmor - figure 2.7) [15].

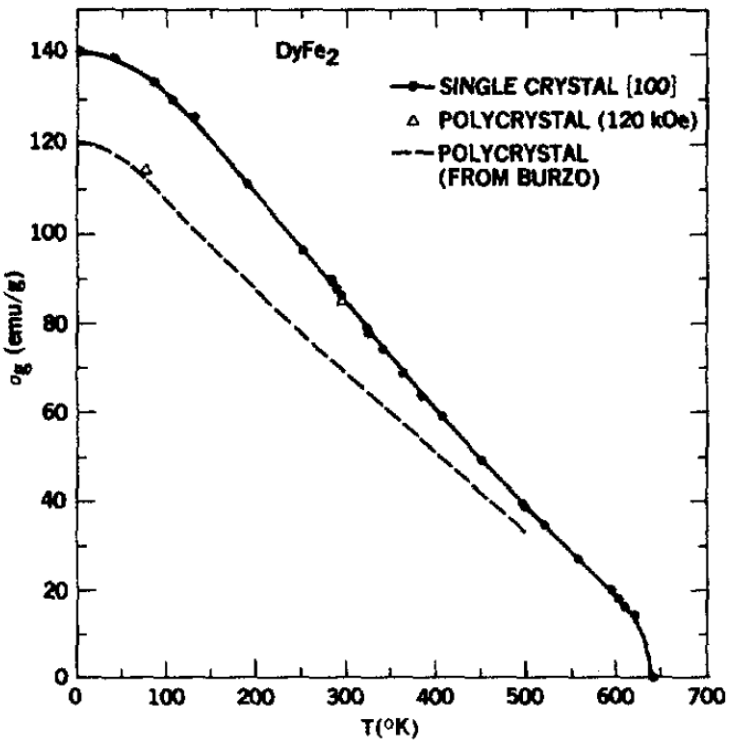

Figure 2.7. Spontaneous magnetic moment (emu/g) of a $DyFe_2$ single crystal as a function of temperature [15].

3. Experimental and computational methods

3.1. Arc melting

The elaboration of rare earth-transition metal intermetallic compounds involves the melting of the components at the stoichiometric composition of the desired compound, either through arc melting or levitation melting [10].

Due to the reaction with crucible materials (Al_2O_3, ThO_2, MgO) at high temperatures, the resistive furnaces are less suitable, since the melt will also contain impurities [10]. Due to this, the arc or levitation melting methods are preferred [10].

Arc melting systems usually contain a high vacuum/argon pumping system [16]. The positive electrode is a water-cooled copper block, with some holes in which the materials are placed [16]. The anode is usually a rod made of tungsten inside the vacuum chamber [16]. The generator provides a high voltage (in the order of kV) to the electrodes, to allow the melting of the compounds [16]. The current is typically in the range of 400-500 A [16]. The removal of impurities from the atmosphere (for example oxygen) can be done by melting some zirconium (or titanium) inside the chamber [16]. To obtain a homogenous sample, multiple melting of the components may be necessary [16]. A typical arc melting system is illustrated in figure 3.1 [7].

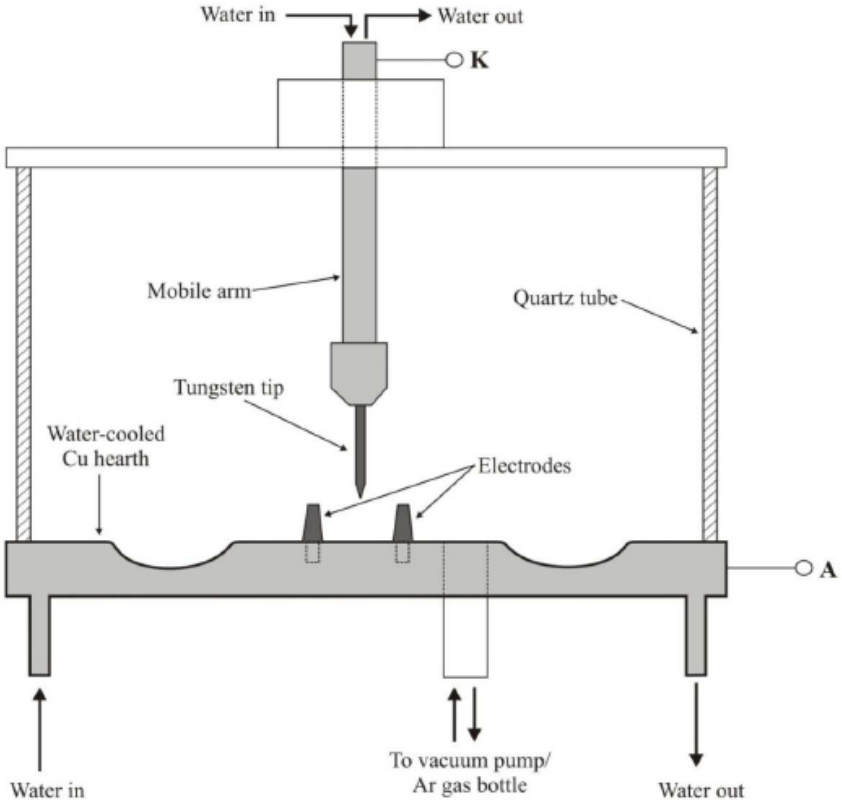

Figure 3.1. Arc melting furnace schematic [7].

After solidification, the obtained sample often consists of a mixture of several intermetallic phases instead of a single one [10]. The sample purity can be further improved through thermal treatments (annealing).

3.2. X-Ray Diffraction

The most common structural characterization method for crystalline solids is X-Ray Diffraction (XRD). This technique is based on Bragg's Law – formula 1.4. X-Ray radiation is suitable for this technique because the interatomic distances are in the order of angstroms and the x-ray radiation wavelength range is of the same order [2].

It should be noted that the Bragg angle θ from the Bragg Law (1.4) is half of the angle of reflection of the incident beam (figure 3.2) [2].

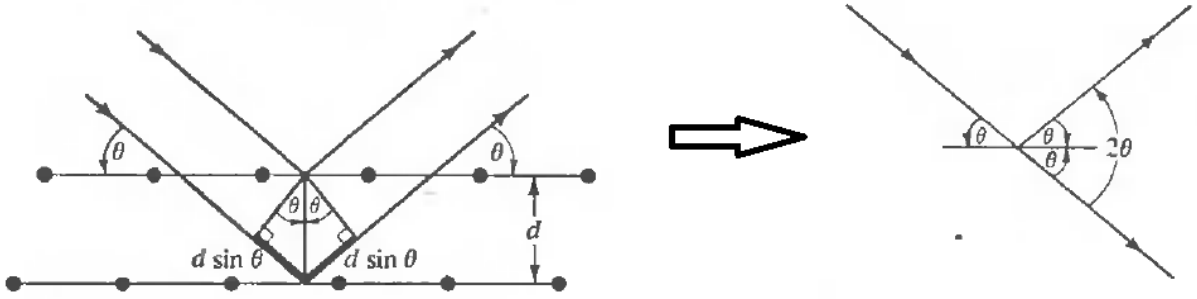

Figure 3.2. The geometry of Bragg scattering [2].

The most common devices used for XRD analysis are powder diffractometers. The basic optics of such a system are presented in figure 3.3 [3].

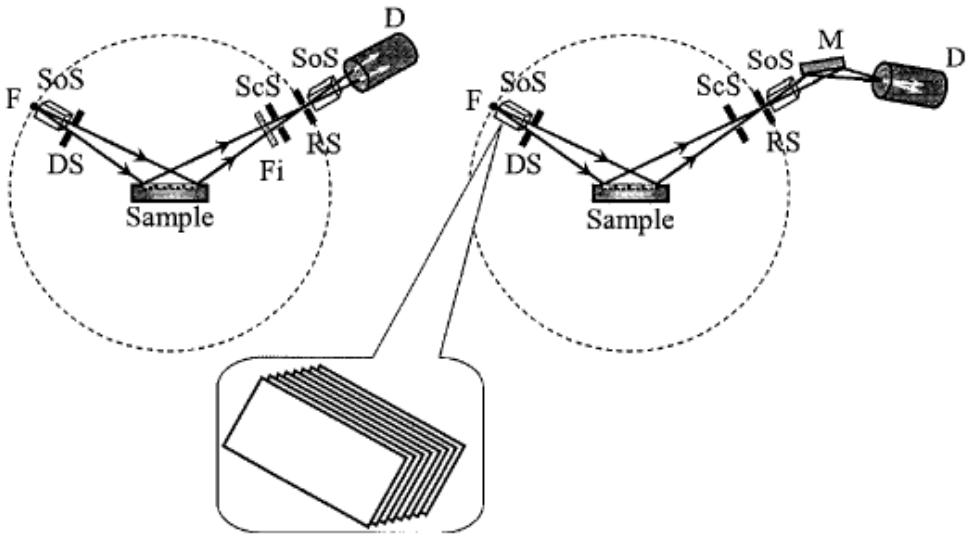

Figure 3.3. Optics of the powder diffractometer: F-focus of the X-ray source, SoS-Soller slits, DS-divergence slit, Fi-beta filter, ScS-scatter slit, RS-receiving slit, M-monochromator, D-detector [3].

The geometry of interest for the structural characterizations required for the current study is the Bragg-Brentano geometry (reflection geometry), summarized in figure 3.4 [3]. A possible drawback of this geometry is that the thickness of the sample must be large enough for it to be opaque to X-rays, therefore it may not be suitable for thin films characterization [3].

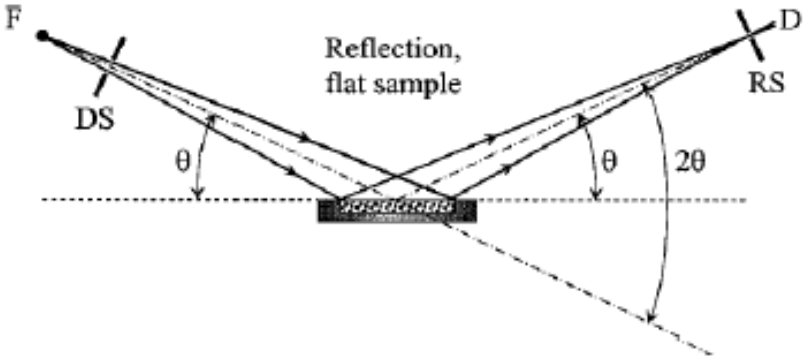

Figure 3.4. Bragg-Brentano focusing geometry [3].

From the diffraction pattern, which is the intensity of the reflected beam as a function of the reflection (or incidence) angle, by using Bragg's Law and structure factor calculations (discussed in chapter 1), several properties, such as the crystallographic information, phase composition and macroscopic structural properties can be determined [3].

3.3. Vibrating sample magnetometry

The vibrating sample magnetometer (VSM) is a type of instrument which relies on the variation of the magnetic flux in a coil in the proximity of a magnetized vibrating sample [17]. The sample is attached to a rod which has the other end fixed to a loudspeaker cone or other type of mechanical vibrator [17]. The quantity of interest is the magnetic moment of the sample, which is proportional to the alternating electromotive force induced in the coils by the oscillating field of the vibrating sample [17]. A schematic of the instrument is provided in figure 3.5 [17].

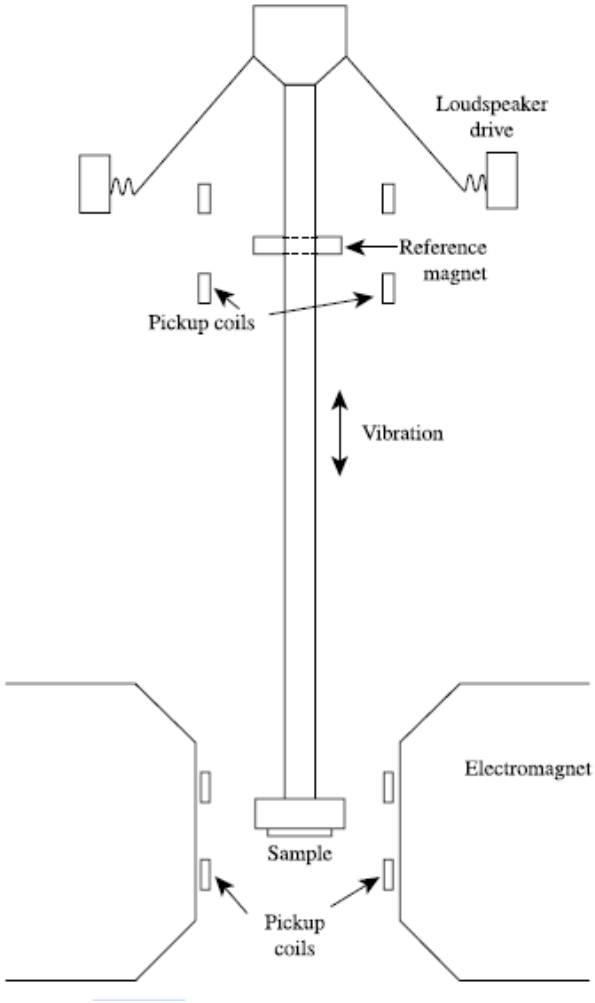

Figure 3.5. Vibrating sample magnetometer [17].

A lock-in amplifier is used for the amplification of the alternating magnetic field [17]. The amplifier is sensitive only to the reference signal, which comes from a sensor coupled to the driving system [17].

The flux generated by the sample is:

$$\phi(t) = MhAsin(\omega t) \tag{3.1}$$

where ϕ is the magnetic flux, M the magnetization of the sample, h is a constant depending on the position of the sample, A is the vibrational amplitude and ω the frequency [6].

The voltage induced in the coils will then be:

$$u(t) = \frac{d\phi}{dt} = c\omega AMcos(\omega t) \tag{3.2}$$

where c is a constant, characteristic for the coils [6].

The reference voltage for the lock-in amplifier is:

$$u_R(t) = c_R\omega AM_Rcos(\omega t) \tag{3.2}$$

where M_R is the reference sample magnetization and c_R the constant of the reference coils [6].

The output voltage of the lock-in amplifier will be:

$$U = kM \tag{3.3}$$

where k is a device dependent constant [6].

3.4. The Weiss balance

The Weiss balance is an instrument based on the Faraday balance, which allows the measurement of the susceptibility of a sample, based on the force which acts on it when placed in an inhomogeneous magnetic field [6]. The magnetic force F acting on the sample is related to the susceptibility χ through:

$$F = \mu_0 m \chi H \frac{dH}{dx} \tag{3.4}$$

where μ_0 is the permeability of vacuum, m the mass of the sample, H the applied field and $\frac{dH}{dx}$ its gradient [6].

The schematic of the system is provided in figure 3.6 [6]. The components of the instrument (from figure 3.6) are: 1 - Electromagnet, 2 - Sample, 3 - Sample holder, 4 - Quartz rod, 5 – Rectangular frame, 6 – Helmholtz coils, 7 – Mirror, 8 – Light source, 9 – Screen, 10 – Hydraulic brake, 11 – Fixed mirror, 12 – Thin, inextensible wires [6]. The purpose of the optical system made of the light source, mirror and screen is the compensation of the displacement of the initial position of the sample due to the magnetic force acting upon it [6]. Bringing the position of the light spot back in the initial position is done through injecting a current in the Helmholtz coils, which will induce a magnetic field, which will be proportional to the force in (3.4) [6]. This will allow the determination of the susceptibility, through some proper calibration [6].

The range of temperatures for the measurements is 77-1300 K in applied fields of up to 1 T [6]. This will allow the determination of important magnetic properties, such as the type of magnetic ordering in the sample, the saturation magnetization and transition temperatures (Curie temperature).

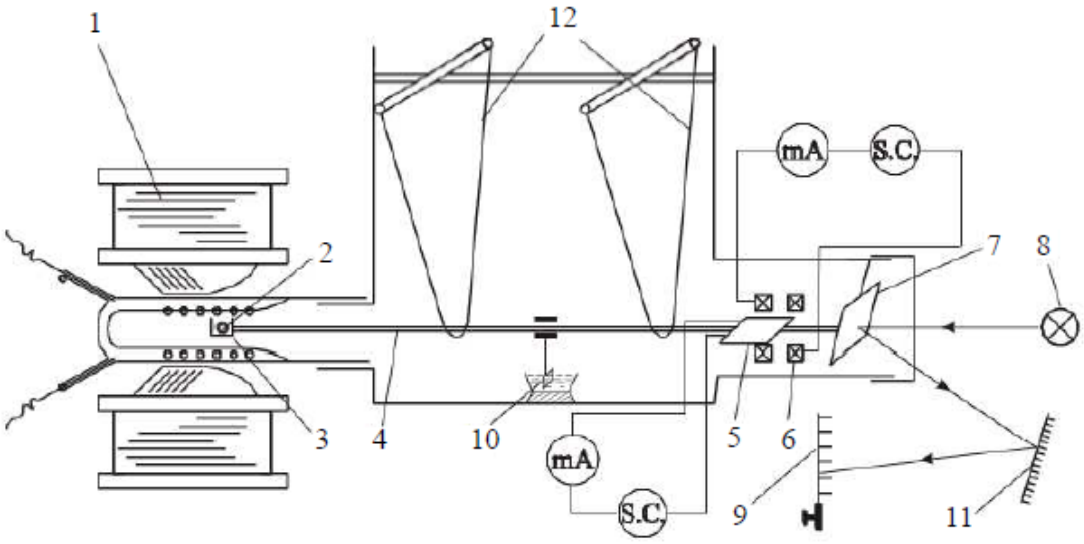

Figure 3.6. Schematic of the Weiss balance [6].

3.5. Computational methods

The challenge in the determination of the ground state properties of a system is that the many-body problem, in which the bodies interact with each other cannot be solved analytically for atoms with more than a few electrons. This gave rise to the necessity of developing numerical methods for solving the Schrödinger equation in the case of many-electron systems. The first development in this field was the Hartree-Fock approximation. A major drawback of this method was that electron correlation effects are neglected [4]. An improved model, density functional theory (DFT) was then developed, based on the work of Hohenberg and Kohn (1964) and Kohn and Sham (1965) [18, 19].

In the Hohenberg and Kohn model, a many-body electron system in an external potential $V_{ext}(\vec{r})$ is considered [4]. The Hamiltonian operator for the system will then be:

$$\hat{H} = -\frac{\hbar^2}{2m_e}\sum_i \nabla_i^2 + \sum_i V_{ext}(\vec{r_i}) + \frac{1}{2}\sum_{i\neq j}\frac{e^2}{(\vec{r_i}-\vec{r_j})} \quad (3.5)$$

where $\hbar$ is the reduced Planck constant, e the charge of the electron and $\vec{r_i}$ the position vector of a given electron [4].

The DFT formalism is based on the Hohenberg-Kohn theorems, which can be formulated in the following way:

Theorem I: For a many electron system, the external potential $V_{ext}(\vec{r})$ is uniquely determined by the ground state electron density $n_0(\vec{r})$ [4].

Corollary: The electron density $n_0(\vec{r})$ will then determine the entirety of the properties of the system [4].

Theorem II: For any external potential $V_{ext}(\vec{r})$, an energy functional $E[n(\vec{r})]$ can be defined. The ground state energy of the system will then be the global minimum of this functional and the corresponding electron density will be the ground state density $n_0(\vec{r})$ [4].

Corollary: The energy functional will determine the ground state energy and electron density [4].

The model on which the most modern electronic structure calculations are based is the Kohn-Sham auxiliary system [4]. The Kohn-Sham assumption (*ansatz*) is that the initial many-body interacting system can be replaced with an independent particle system with an interacting density, described by an exchange correlation energy functional $E_{XC}[n]$ [4]. In the context of the Hohenberg and Kohn theorems, the auxiliary system model will provide the ground state energy and density of the original many-body interacting system [4]. Therefore, even though the exact wavefunction of individual electrons is not determined, the ground state properties of the system can still be determined through the ground state electron density.

In the Kohn-Sham auxiliary system, two main assumptions are made:

i) The ground state density of the system can be replaced by the ground state of an auxiliary non-interacting particle system [4].

ii) The Hamiltonian of the auxiliary system will contain a kinetic energy operator and a local effective potential $V_{eff}^{\sigma}(\vec{r})$ acting on an electron with spin σ at the corresponding point in space [4].

The Hamiltonian is then formulated as:

$$\widehat{H}_{aux}^{\sigma} = -\frac{1}{2}\nabla^2 + V^{\sigma}(\vec{r}) \tag{3.6}$$

In formula 3.6, the Hartree atomic units are used, for simplification ($\hbar = m_e = \frac{4\pi}{\varepsilon_0} = 1$) [4].

The electron density in this approximation is given by the wavefunctions of orbitals corresponding to each spin $\psi_i^{\sigma}(\vec{r})$ [4]:

$$n(\vec{r}) = \sum_{\sigma} n(\vec{r},\sigma) = \sum_{\sigma}\sum_{i=1}^{N^{\sigma}} |\psi_i^{\sigma}(\vec{r})|^2 \tag{3.7}$$

The corresponding kinetic energy is then [4]:

$$T_S = -\frac{1}{2}\sum_{\sigma}\sum_{i=1}^{N^{\sigma}} \langle\psi_i^{\sigma}|\nabla^2|\psi_i^{\sigma}\rangle = -\frac{1}{2}\sum_{i=1}^{N^{\sigma}} \int d^3r |\nabla\psi_i^{\sigma}(\vec{r})|^2 \tag{3.8}$$

The Coulomb interaction energy (Hartree energy) as a function of electron density is [4]:

$$E_{Hartree}[n] = \frac{1}{2}\int d^3r d^3r' \frac{n(\vec{r})n(\overrightarrow{r'})}{|\vec{r}-\overrightarrow{r'}|} \tag{3.9}$$

In the Kohn-Sham auxiliary system, the ground state energy functional can be written as [4]:

$$E_{KS} = T_S[n] + \int d\,\vec{r} V_{ext}(\vec{r}) n(\vec{r}) + E_{Hartree}[n] + E_{II} + E_{XC}[n] \quad (3.10)$$

where E_{II} is the interaction energy between nuclei, $E_{XC}[n]$ is the previously mentioned exchange correlation functional and $V_{ext}(\vec{r})$ the external potential to which the electrons are subjected [4].

The exchange-correlation functional term contains the many-body interaction effects of exchange and correlation [4]:

$$E_{XC}[n] = F_{HK}[n] - (T_S[n] + E_{Hartree}[n]) \quad (3.11)$$

where $F_{HK}[n]$ is the Hohenberg-Kohn functional, which contains the internal energies (kinetic and potential) of the interacting system [4]:

$$F_{HK}[n] = T[n] + E_{int}[n] \quad (3.12)$$

Equation 3.11 can then be expressed as [4]:

$$E_{XC}[n] = \langle \hat{T} \rangle - T_S[n] + \langle \widehat{V_{int}} \rangle - E_{Hartree}[n]) \quad (3.13)$$

The solution of this system is determined by typical variational principles, such as the minimization of the energy with respect to either the electron density or the effective potential [4]. This approach leads to the Kohn-Sham equations:

$$(H_{KS}^{\sigma} - \varepsilon_i^{\sigma})\, \psi_i^{\sigma}(\vec{r}) = 0 \quad (3.14)$$

where H_{KS}^{σ} is the auxiliary system effective Hamiltonian (from equation 3.6) [4]:

$$H_{KS}^{\sigma}(\vec{r}) = -\frac{1}{2}\nabla^2 + V_{KS}^{\sigma}(\vec{r}) \quad (3.15)$$

The Kohn-Sham potential is [4]:

$$V_{KS}^{\sigma}(\vec{r}) = V_{ext}(\vec{r}) + \frac{\delta E_{Hartree}}{\delta n(\vec{r},\sigma)} + \frac{\delta E_{XC}}{\delta n(\vec{r},\sigma)} = V_{ext}(\vec{r}) + V_{Hartree}(\vec{r}) + V_{XC}^{\sigma}(\vec{r}) \quad (3.16)$$

The equations are solved through a self-consistent method, based on an initial guess of the electron density or the potential $V_{eff}^{\sigma}(\vec{r})$ [4]. Successive variation of these quantities are performed until consistency between them (self-consistency) is reached [4]. A general diagram of a self-consistent loop for solving the Kohn-Sham equations is provided in figure 3.7 [4].

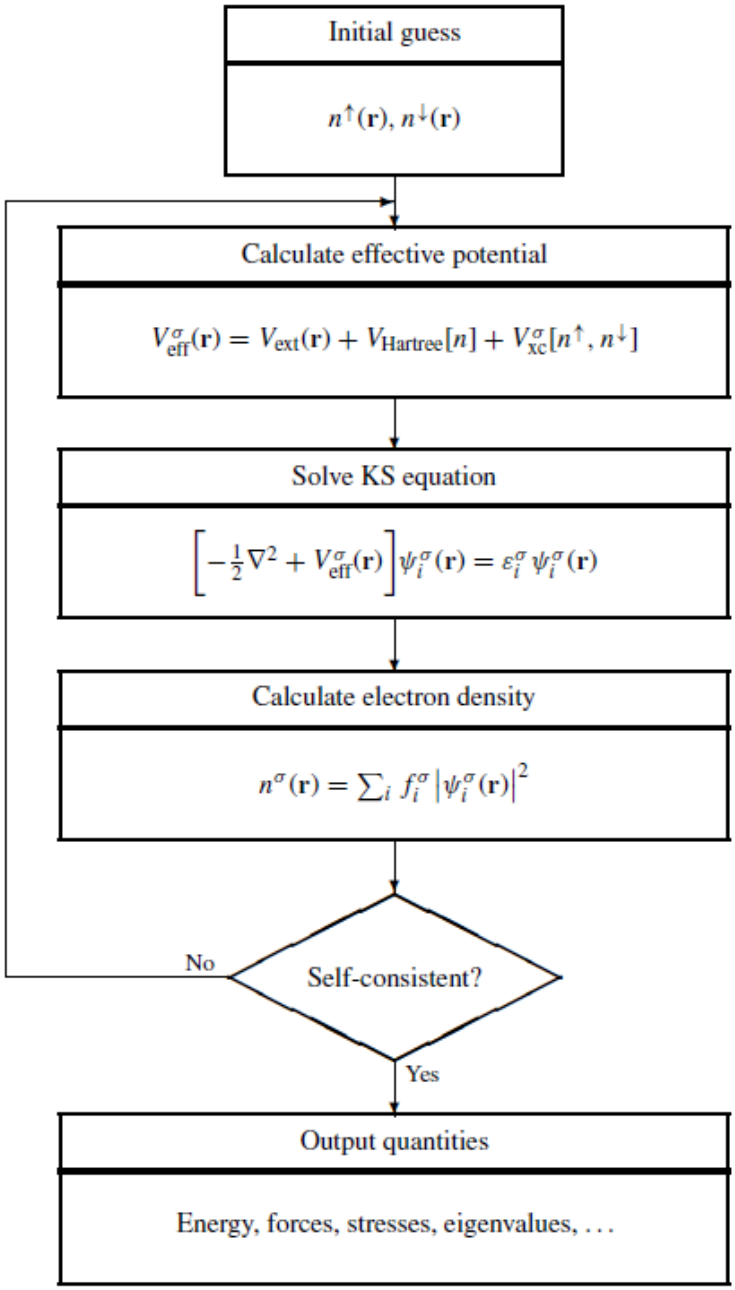

Figure 3.7. Self-consistent loop [4].

Since many-body interactions are described by the exchange-correlation functional, a fundamental step in self-consistent calculations is the choice of an appropriate approximation of this functional. A successful approximation is the generalized gradient approximation (GGA).

The GGA approximation proposes an expansion of the exchange correlation functional in terms of the gradient of the electron density $|\nabla n^{\sigma}|$ and the electron density n at each point, with the following general expressions:

$$E_{xc}^{GGA} = \int d^3r\, n(r)\, \epsilon_{xc}\left(n^{\uparrow}, n^{\downarrow}, \left|\nabla n^{\uparrow}\right|, \left|\nabla n^{\downarrow}\right|, \dots\right) \tag{3.17}$$

$$E_{xc}^{GGA} = \int d^3r\, n(r)\, \epsilon_x^{hom}(n)\, F_{xc}\left(n^{\uparrow}, n^{\downarrow}, \left|\nabla n^{\uparrow}\right|, \left|\nabla n^{\downarrow}\right|, \dots\right) \tag{3.18}$$

where F_{xc} is dimensionless and $\epsilon_x^{hom}(n)$ is the exchange energy of the unpolarized gas [4].

The potential $V_{xc}^{\sigma}(r)$ can be determined as the term in the brackets from [4]:

$$\delta E_{xc}[n] = \sum_{\sigma} \int dr \left[\epsilon_{xc} + n\frac{\partial \epsilon_{xc}}{\partial n^{\sigma}} + n\frac{\partial \epsilon_{xc}}{\partial \nabla n^{\sigma}}\nabla\right]_{r,\sigma} \delta n(r,\sigma) \tag{3.19}$$

$$V_{xc}^{\sigma}(r) = \left[\epsilon_{xc} + n\frac{\partial \epsilon_{xc}}{\partial n^{\sigma}} - \nabla\left(n\frac{\partial \epsilon_{xc}}{\partial \nabla n^{\sigma}}\right)\right]_{r,\sigma} \tag{3.20}$$

A limitation of the Kohn-Sham approach is systems in which the electrons are localized and strongly interacting (for example transition metal oxides and rare earth elements and compounds) [4]. The DFT+U correction brings an additional orbital dependent contribution which successfully addresses this issue [4]. Therefore, the new exchange interaction energy term will become:

$$E_{xc}^{GGA+U} = E_{xc}^{GGA} + E_U\left[n_m^{I,\sigma}\right] - E_{DC}[n^{I,\sigma}] \tag{3.21}$$

where $n_m^{I,\sigma}$ is the atomic orbital occupations with spin σ for the correlated atom I and E_{DC} is a double counting term which removes the same amount of Coulomb repulsion already contained in the Hamiltonian [20].

The orbital interaction term is:

$$E_U[n(\vec{r})] = \frac{1}{2}\sum_{\{m\},I,\sigma}[\langle m,m''|V_{ee}|m',m'''\rangle n_{mm'}^{I,\sigma} n_{m''m'''}^{I,-\sigma} + (\langle m,m''|V_{ee}|m',m'''\rangle - \langle m,m''|V_{ee}|m''',m'\rangle) n_{mm'}^{I,\sigma} n_{m''m'''}^{I,-\sigma} \tag{3.22}$$

where V_{ee} corresponds to the screened electrostatic interactions between the localized electrons [20].

For simplification of solving the Kohn-Sham equation, the strong Coulomb potential of the nucleus and the tightly bound core electrons are replaced by an effective ionic potential acting on valence electrons in the form of a pseudopotential [4]. A condition for the pseudopotential to be accurate and transferable to different calculations is that it should be "norm-conserving" [4]. This is expressed in the orthonormality condition:

$$\left\langle \psi_i^{\sigma,PS} \middle| \psi_j^{\sigma',PS} \right\rangle = \delta_{i,j}\,\delta_{\sigma,\sigma'} \tag{3.23}$$

where $\psi^{PS}(r)$ are the wavefunctions corresponding to the pseudopotential [4]. This will lead to the new form of the Kohn-Sham equations:

$$\left(H_{KS}^{\sigma,PS} - \varepsilon_i^{\sigma}\right)\psi_i^{\sigma,PS}(r) = 0 \tag{3.24}$$

where the external potential will be determined by the norm conserving condition [4].

The minimum requirements for a "shape consistent" and "norm conserving" pseudopotential were given by Hamann, Schluter, and Chiang [4]:

1. "All-electron and pseudo valence eigenvalues agree for the chosen atomic reference configuration." [4]
2. "All-electron and pseudo valence wavefunctions agree beyond a chosen core radius Rc" [4]
3. "The logarithmic derivatives of the all-electron and pseudo wavefunctions agree at R_c" [4]
4. "The integrated charge inside R_c for each wavefunction agrees (norm-conservation)" [4]
5. "The first energy derivative of the logarithmic derivatives of the all-electron and pseudo wavefunctions agrees R_c, and therefore for all $r \geq R_c$" [4]

To obtain "smoother" pseudopotentials while preserving accuracy, a different approach, in the form of "ultrasoft" pseudopotentials was developed [4]. This is done by introducing some "smooth" wavefunctions $\tilde{\psi}_i$, which are not norm-conserving [4]. The general eigenvalue problem is then described by:

$$\left[-\frac{1}{2}\nabla^2 + V_{local} + \delta\hat{V}_{NL}^{US} - \varepsilon_i\hat{S}\right]\tilde{\psi}_i = 0 \tag{3.25}$$

where $\delta\hat{V}_{NL}^{US}$ is a new non-local potential acting on $\tilde{\psi}_i$ and $\hat{S}$ is an overlapping operator [4]. $\hat{V}_{NL}^{US}$ is an approximation of the potential acting on the valence states in the molecule or solid [4].

A modern method for electronic structure calculation is the projector augmented wave (PAW) method. In this method, a smooth part of a valence wavefunction or atomic orbital $\widetilde{\psi^v}$, which is related to the original wavefunction through a linear transformation [4]:

$$\psi^v = \mathrm{T}\widetilde{\psi^v} \tag{3.26}$$

This can be expressed in the Dirac notation by:

$$|\tilde{\psi}\rangle = \sum_m c_m |\tilde{\psi}_m\rangle \tag{3.27}$$

with the original wavefunctions [4]:

$$|\psi\rangle = \mathrm{T}|\tilde{\psi}\rangle = \sum_m c_m |\psi_m\rangle \tag{3.28}$$

Therefore, the full wavefunction can be expressed as [4]:

$$|\psi\rangle = |\tilde{\psi}\rangle + \sum_m c_m \{|\psi_m\rangle - |\tilde{\psi}_m\rangle\} \tag{3.29}$$

Since the transformation T is linear, the c_m coefficients must be determined by some set of projection operators $\tilde{p}$ [4]:

$$c_m = \langle\tilde{p}_m|\tilde{\psi}\rangle \tag{3.30}$$

From the orthogonality condition we have [4]:

$$\langle\tilde{p}_m|\tilde{\psi}_{m'}\rangle = \delta_{mm'} \tag{3.31}$$

The transformation can be then expressed as [4]:

$$\mathrm{T} = 1 + \sum_m \{|\psi_m\rangle - |\tilde{\psi}_m\rangle\}\langle\tilde{p}_m| \tag{3.32}$$

The PAW equations can then be expressed in terms of the transformation operator in equation 3.32 [4]. This will provide the following expression for the electron density:

$$n(r) = \tilde{n}(r) + n^1(r) - \tilde{n}^1(r) \tag{3.33}$$

where $\tilde{n}(r)$ can be expressed in terms of the eigenstates i with the occupations f_i [4]:

$$\tilde{n}(r) = \sum_i f_i \, |\tilde{\psi}_i(r)|^2 \tag{3.34}$$

The $n^1(r)$ and $\tilde{n}^1(r)$ terms are localized around each atom and can be expressed as [4]:

$$n^1(r) = \sum_i f_i \sum_{mm'} \langle \tilde{\psi}_i | \tilde{\psi}_m \rangle \psi_m^*(r) \psi_{m'}(r) \langle \tilde{\psi}_{m'} | \tilde{\psi}_i \rangle \tag{3.35}$$

and

$$\tilde{n}^1(r) = \sum_i f_i \sum_{mm'} \langle \tilde{\psi}_i | \tilde{\psi}_m \rangle \tilde{\psi}_m^*(r) \tilde{\psi}_{m'}(r) \langle \tilde{\psi}_{m'} | \tilde{\psi}_i \rangle \tag{3.36}$$

The energy of the system can be expressed in a similar way:

$$E_{total} = \tilde{E}_{total} + E^1_{total} + \tilde{E}^1_{total} \tag{3.37}$$

where $\tilde{E}$ is the energy due to the smooth functions evaluated in Fourier space or a grid that extends throughout space, $\tilde{E}^1$ the same terms evaluated only in the spheres on radial grids and the energy in the spheres with the full functions is denoted as E^1 [4].

4. Results and discussions

The purpose of the computational work was to determine some of the main structural and magnetic properties of the $DyFe_{2-x}Cu_x$ compounds. The calculations were performed using the Abinit software package [21]. The PAW method was used [22]. The Perdew, Burke and Ernzherof (PBE) exchange correlation functional, in the GGA approximation was chosen [23, 24]. For the optimization of computational time, the Niggli-reduced primitive cell from figure 4.1 was used as an input structure [25]. The lattice parameters are $a = b = c = 5.176$ Å and the primitive vector angles $\alpha = \beta = \gamma = 60$ °. The positions of the atoms are provided in table 4.1. The electronic structure calculations were spin-polarized and the datasets from the JTH library were used for the PAW GGA implementation [26]. A 6x6x6 k-point grid with a cutoff energy of 25 Ha was used. Due to the strong electron correlation, a DFT+U correction for the 4f electrons was necessary with U=8eV and J=1.1eV [27].

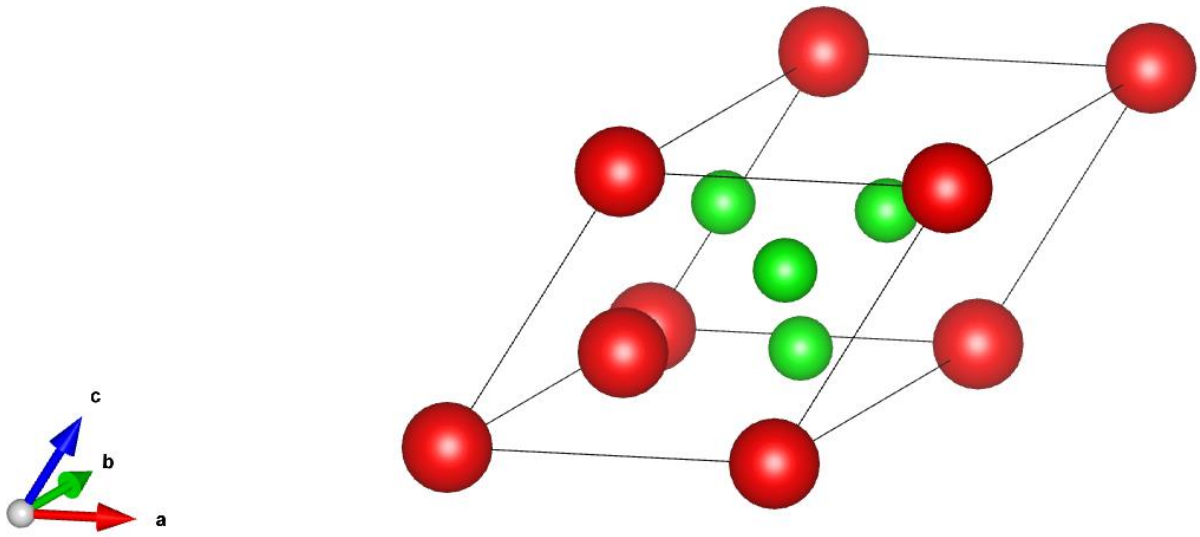

Figure 4.1. Primitive cell of the $DyFe_2$ intermetallic compound with Dy in red and Fe in green [11].

Table 4.1. Atomic positions in the primitive cell.

Atom	*x*	*y*	*z*
Dy_1	0	0	0
Dy_2	0.25	0.25	0.25
Fe_1	0.125	0.625	0.625
Fe_2	0.625	0.125	0.625
Fe_3	0.625	0.625	0.125
Fe_4	0.625	0.625	0.625

The density of states (DOS) for the $DyFe_{2-x}Cu_x$ compounds, with x=0, 0.5, 1 and 1.5 were computed and plotted in figures 4.2 – 4.5. The effect of the copper doping on the magnetic properties of the compound can be explained by the change in the DOS with the concentration x.

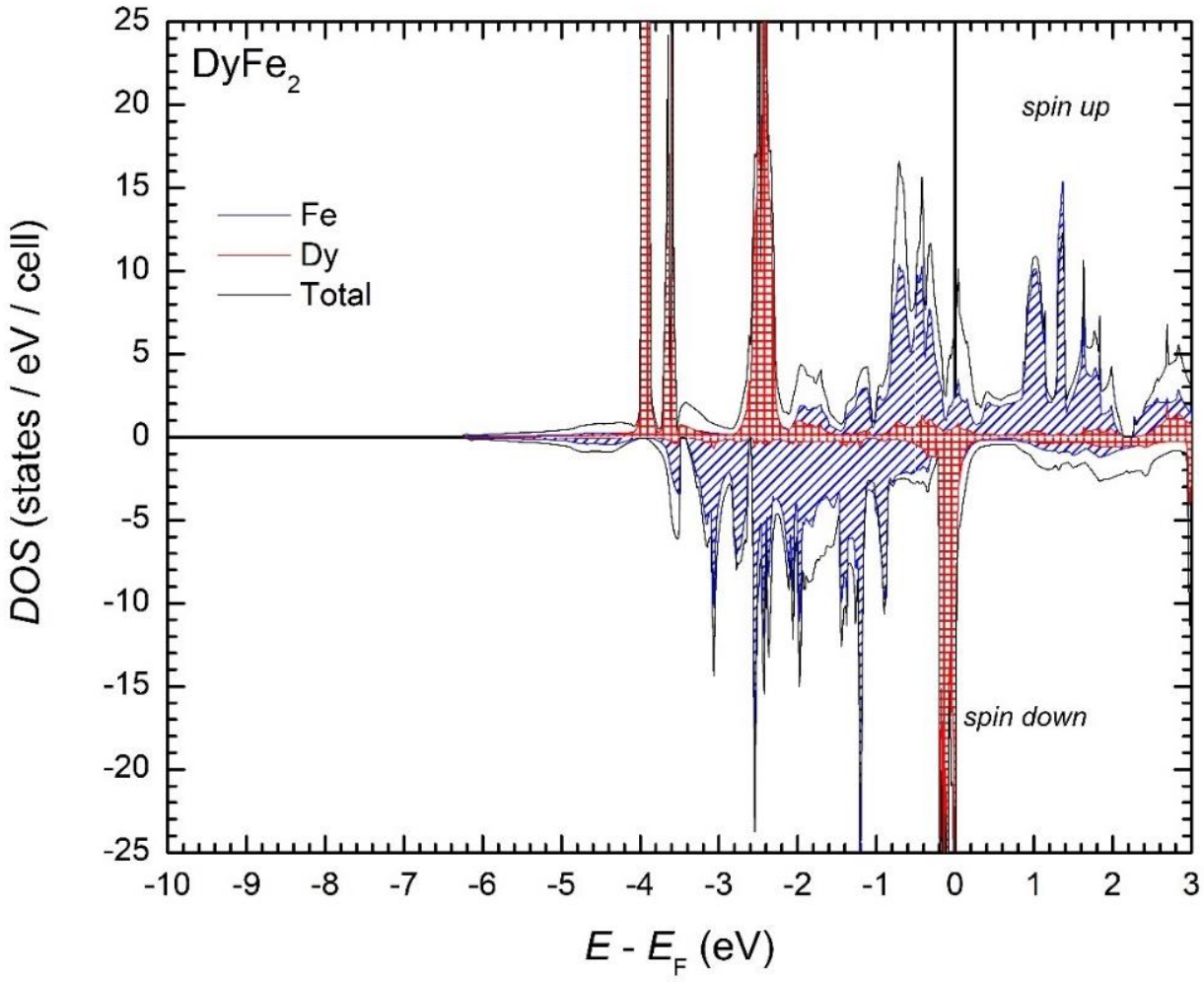

Figure 4.2. Computed density of states for the $DyFe_2$ compound.

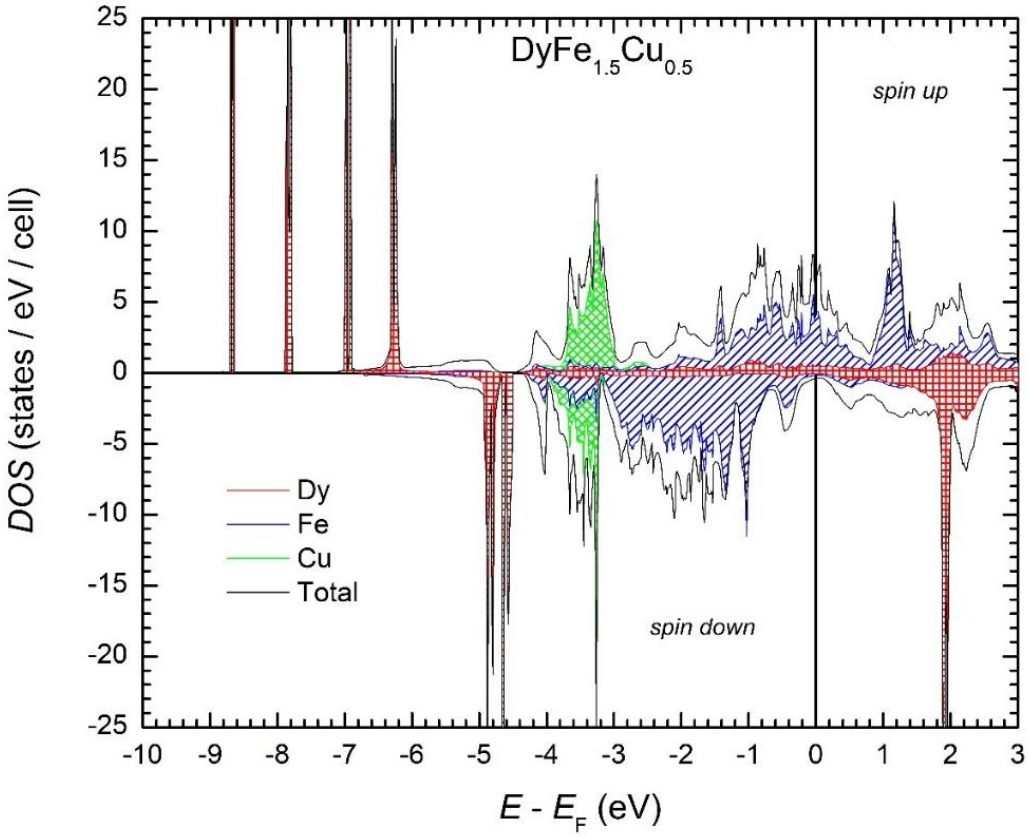

Figure 4.3. Computed density of states for the $DyFe_{1.5}Cu_{0.5}$ compound.

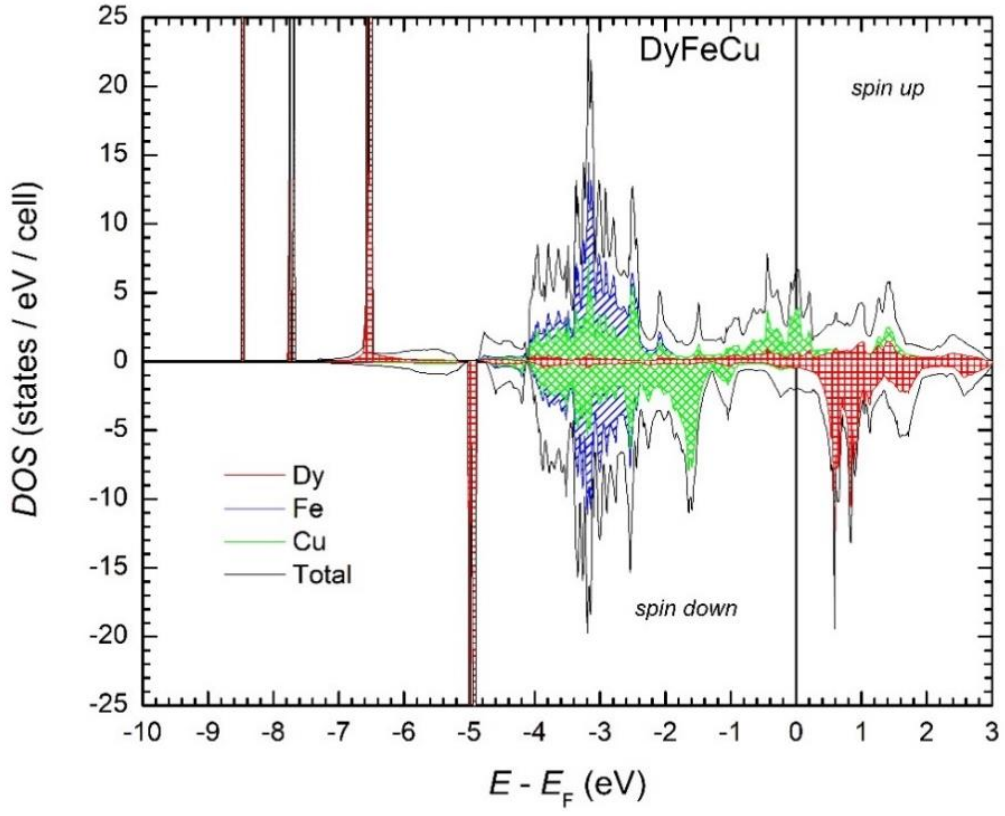

Figure 4.4. Computed density of states for the DyFeCu compound.

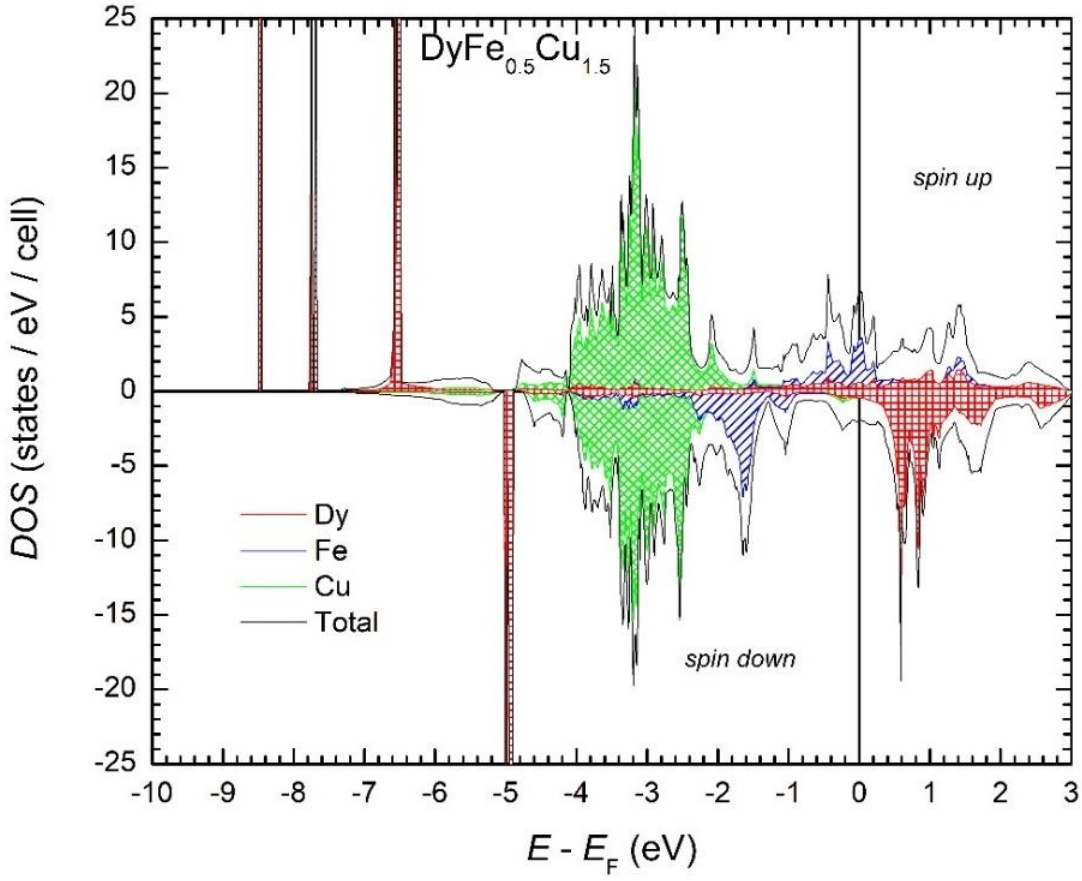

Figure 4.5. Computed density of states for the $DyFe_{0.5}Cu_{1.5}$ compound.

When the copper concentration increases from $x = 0$ to $x = 0.5$, a splitting in the 4*f* bands takes place. This leads to the increase of the Dy atomic magnetic moments. Along with the increase of the copper concentration, the Fe 3*d* bands are being progressively filled which leads to a decrease in the atomic magnetic moments of Fe. The lattice parameters and magnetic moments calculated from the DFT simulations are provided in table 4.2.

Table 4.2. Lattice parameters (a) and individual and total magnetic moments for concentrations of copper ranging from $x = 0$ to $x = 1.5$.

x	a (Å)	m_{Dy} (μ_B / atom)	m_{Fe} (μ_B / atom)	m_{Cu} (μ_B / atom)	m_{total} (μ_B / cell)	m_{total} (μ_B / f.u.)
0.0	5.21	4.53	-2.25	-	0.72	0.36
0.5	5.19	5.31	-2.15	-0.08	5.02	2.51
1.0	5.20	5.29	-1.92	0.00	7.62	3.81
1.5	5.25	5.20	-1.98	0.01	9.08	4.54

The lattice parameter *a* does not present a significant variation with the copper concentration. This result was expected, since the atomic radii of Fe and Cu are almost equal, with 1.274 Å for iron and 1.278 Å for copper [28]. The Dy atomic magnetic moment increases initially, from la 4.53 μ_B/atom to 5.31 μ_B/atom when *x* increases from 0 to 0.5, but then decreases to 5.20 μ_B/atom for $x = 1.5$. The magnetic moments of the iron atoms are slightly decreasing with the increase of the copper concentration. The total magnetic moment increases proportionally with the copper concentration. This behaviour was expected, given the evolution of the denisty of states, discussed above. Therefore, the increase in total magnetic moment can be explained through magnetic dilution and the decrease of the Fe magnetic moments. However, it is worth mentioning that the Dy magnetic moments are likely underestimated, due to the Abinit code limitations. The software package is based on plane waves and pseudopotential and does not account for the spin-orbit coupling, meaning that the orbital magnetic moment was not taken into consideration.

Along with the computational studies, experimental characterization of the structural and magnetic properties of the compounds were also performed. Several samples with the copper concentration x in the $0 \leq x \leq 1.5$ range were elaborated through the arc melting method (discussed in chapter 3) in an Ar inert atmosphere. In order to compensate the evaporation losses during the melting process, an additional 1% of Dy was added. The samples were melt multiple times to ensure homogeneity. After the casting, the samples were subjected to thermal treatment (annealing) in tantalum foil under vacuum at 950 °C for 4 days.

The X-ray characterization of the samples was performed using the Bruker D8 Advance diffractometer, with the Cu Kα radiation wavelength. The resulting diffraction patterns for the samples, as cast and annealed are provided in figures 4.6 and 4.7 respectively. The as-cast samples are all phase mixtures containing $DyFe_2$ and $DyFe_3$-type phases. The pattern in figure 4.7 is much smoother, indicating that the annealing process lead to better homogeneity and crystallinity of the samples. For the $0 \leq x \leq 0.4$ copper concentration range, the samples presented a majority $DyFe_2$ type phase, indicated by the peaks corresponding to the $DyFe_2$ planes (figure 4.8) and a minority $DyFe_3$ phase in a very low concentration which can be identified by the additional low intensity peaks. In the $0.5 \leq x < 1$ range, the intensity of the peaks corresponding to the $DyFe_3$ phase increases, leading to a phase mixture. For $1 \leq x \leq 1.5$, the $DyFe_3$ are dominant, leading to a $DyFe_3$ majority phase. The formation enthalpies of $DyFe_2$ and DyFe3 are very close [29]. The addition of copper will cause a shift in the formation enthalpy of the $DyFe_3$ phase, causing it to decrease, therefore, this phase will become more stable than the $DyFe_2$ phase. This can be concluded from figure 4.9, where it can be seen that the intensity of the peaks corresponding to the $DyFe_2$ phase

decrease with the increasing of *x* and new peaks of increasing intensity, corresponding to the $DyFe_3$ phase emerge and become dominant for *x*=1.5.

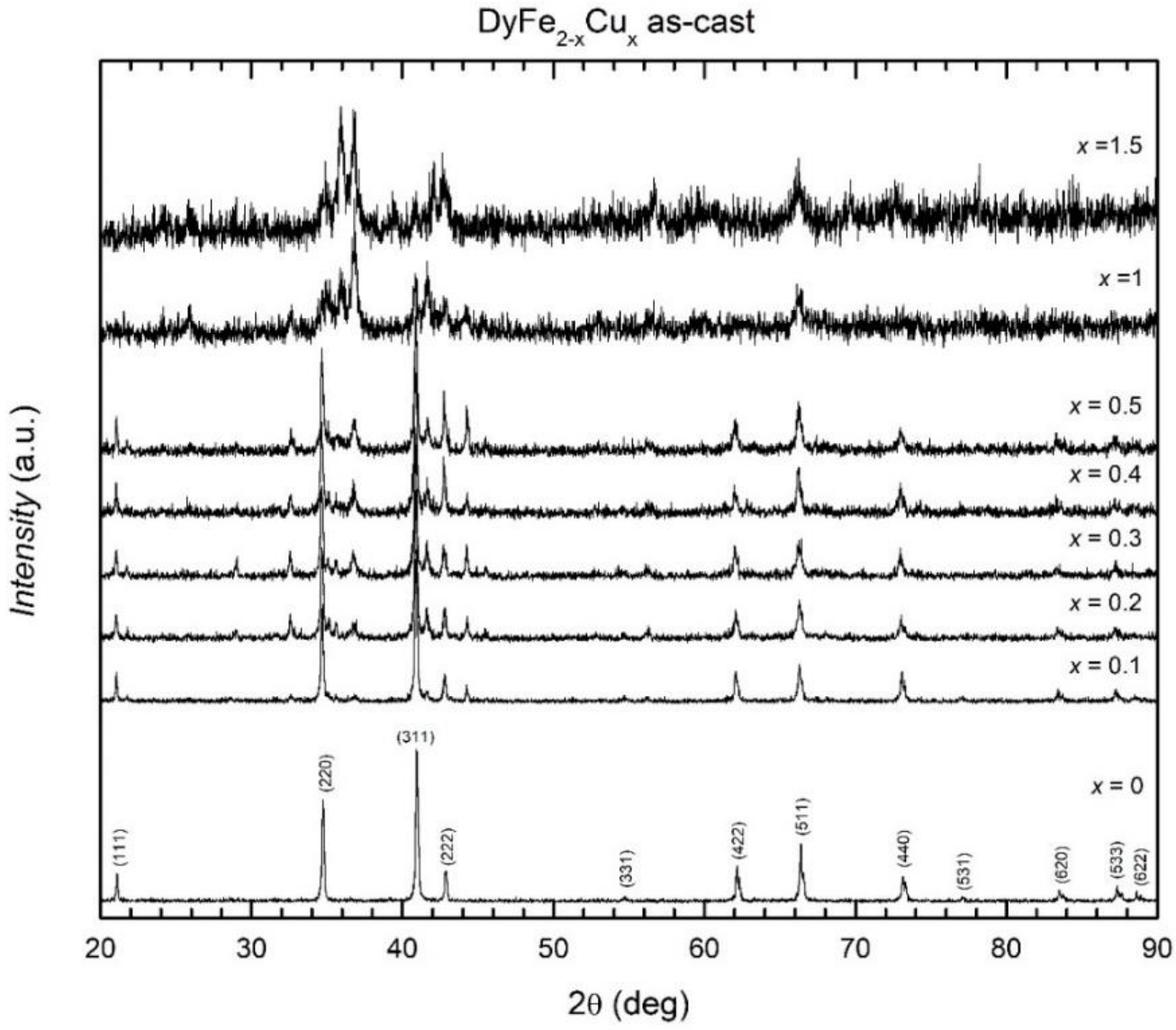

Figure 4.6. X-ray diffraction patterns for the $DyFe_{2-x}Cu_x$ compounds for $0 \leq x \leq 1.5$ - as cast.

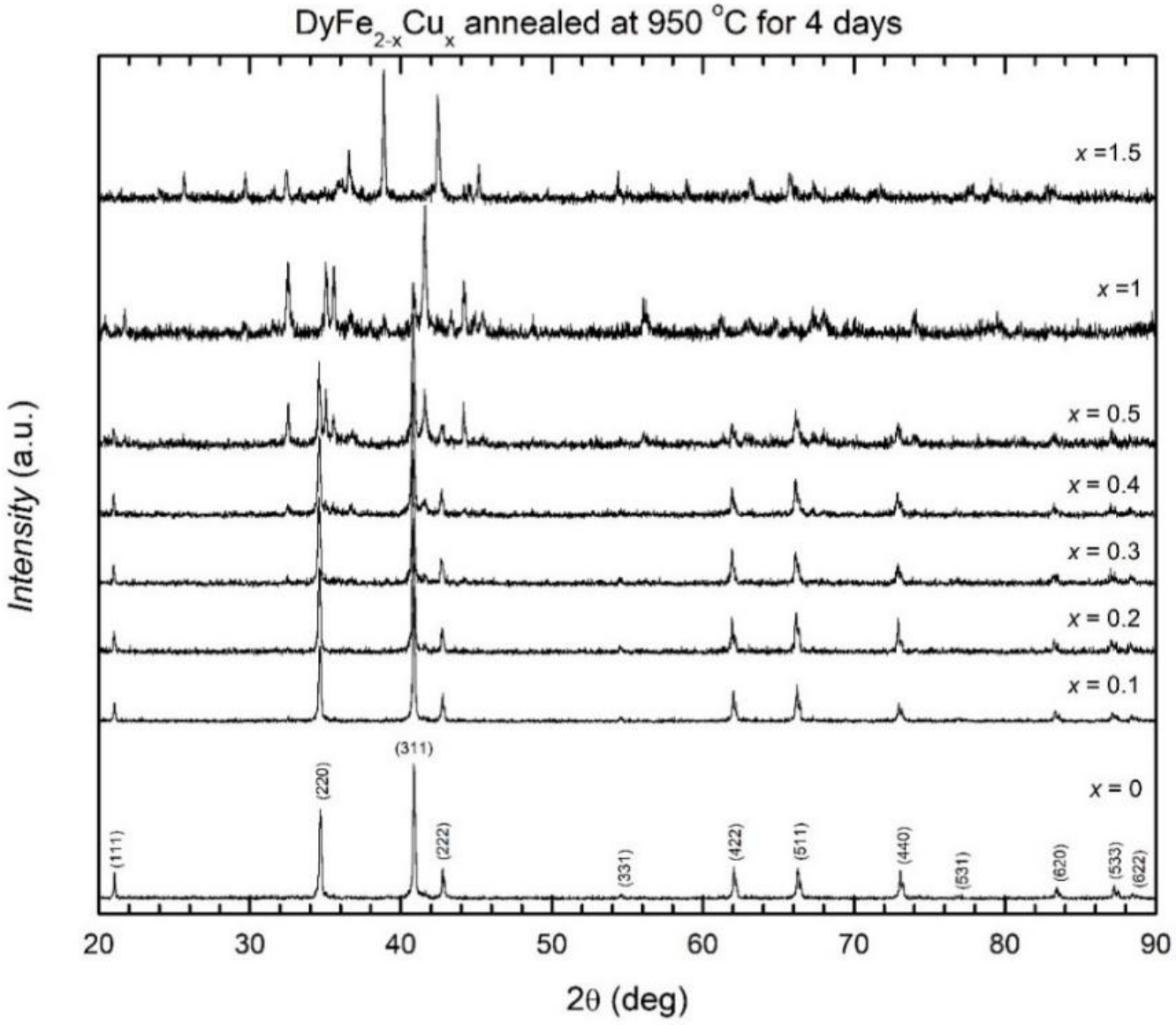

Figure 4.7. X-ray diffraction patterns for the $DyFe_{2-x}Cu_x$ compounds for $0 \leq x \leq 1.5$ after annealing at 950 °C for 4 days.

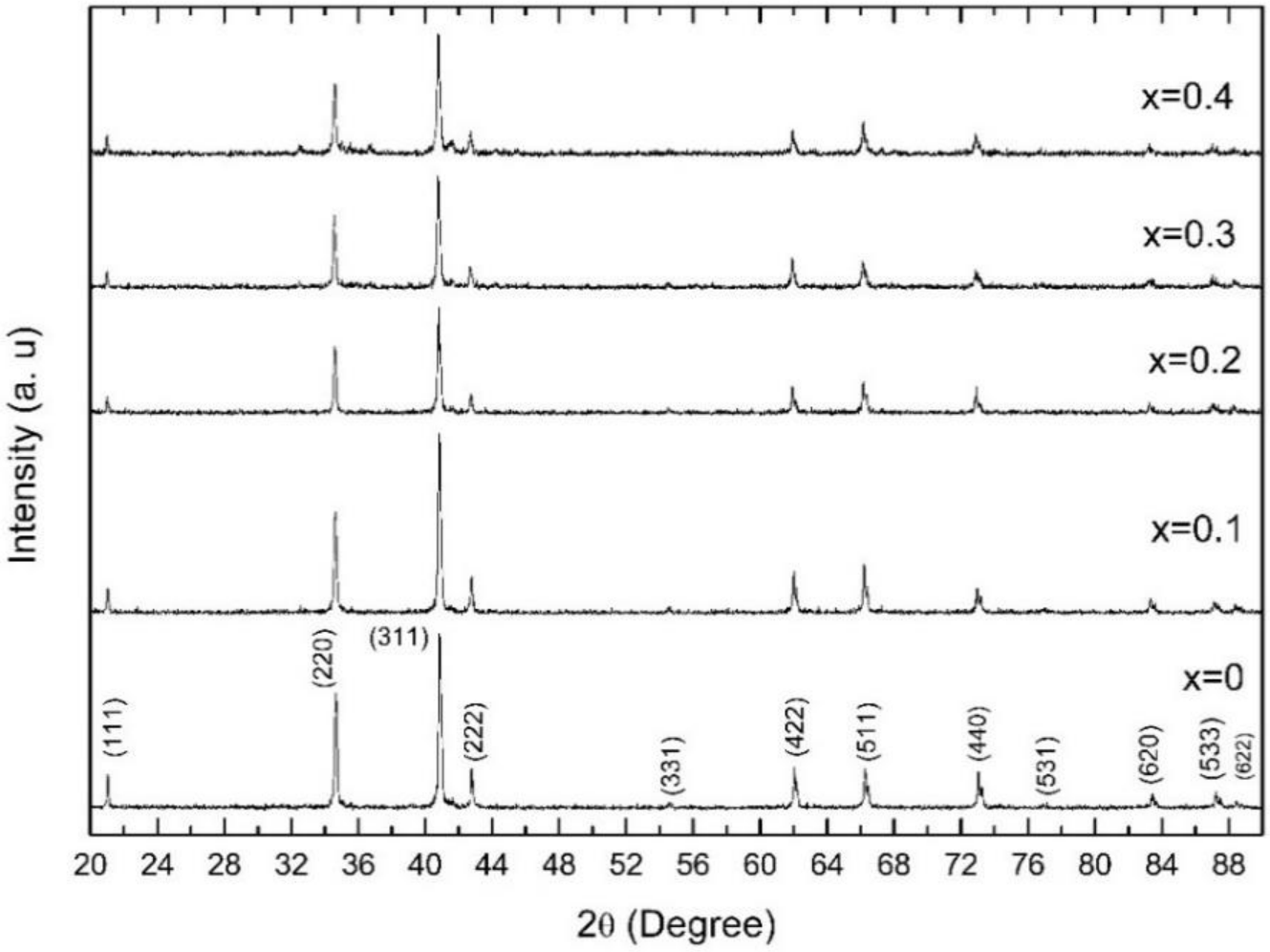

Figure 4.8. X-ray diffraction patterns for the annealed $DyFe_{2-x}Cu_x$ compounds for $0 \leq x \leq 0.4$. The Miller indices corresponding to the $DyFe_2$ compound are indicated at the bottom.

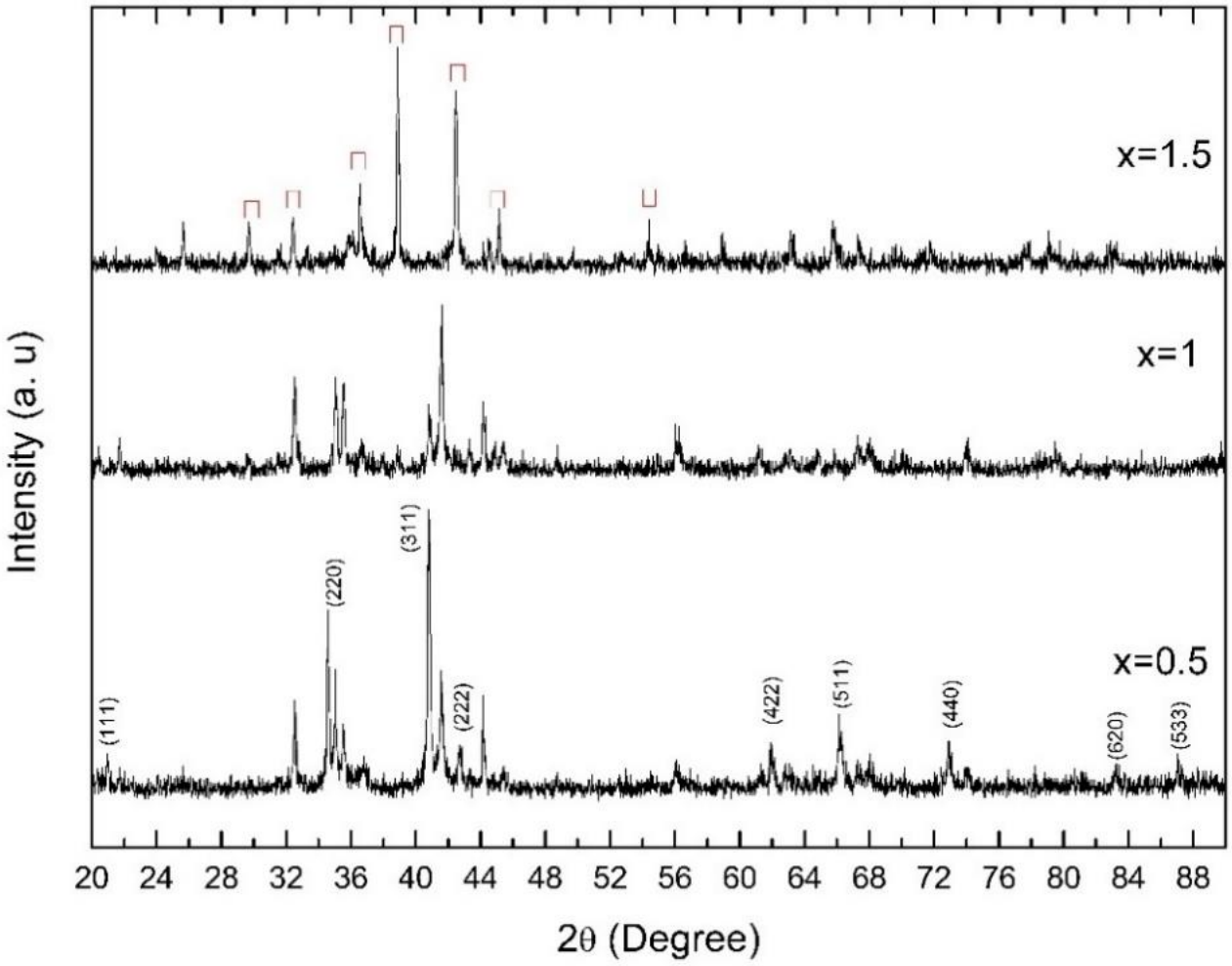

Figure 4.9. X-ray diffraction patterns for the annealed $DyFe_{2-x}Cu_x$ compounds for $0.5 \leq x \leq 1.5$. The Miller indices corresponding to the $DyFe_2$ compound are indicated in the brackets and the some of the peaks corresponding to the $DyFe_3$ compound are marked by the red squares.

The experimentally determined lattice parameter values for the conventional and primitive cell are provided in table 4.3. As expected from the computational results, the copper concentration does not significantly alter the lattice parameter of the compound. Also, the experimental values are in good agreement with the values from the DFT calculations.

The magnetic properties of the samples were investigated using a vibrating sample magnetometer (VSM) in the 4-300 K temperature range and in applied fields of up to 12T. Thermomagnetic curves were obtained using a Weiss-Faraday balance in the 300-800K temperature domain.

Table 4.3. Experimental lattice parameters for the conventional and primitive cells.

x	a_{conv}	a_{prim}
0	7.32	5.17
0.1	7.33	5.18
0.2	7.33	5.18
0.3	7.34	5.19
0.4	7.34	5.19

The saturation magnetization was determined by fitting the experimental data with the relation:

$$M = M_S\left(1 - \frac{b}{H}\right) + \chi_0 H \tag{4.1}$$

where M is the magnetization, M_S the saturation magnetization, b the magnetic hardness coefficient and χ_0 a Pauli-type contribution [17]. The experimental magnetization isotherms that were used are presented in figure 4.10.

The Curie temperature was determined as the point at which the derivative of the magnetization with respect to temperature is a minimum. This was done by fitting the thermomagnetic curves, provided in figure 4.11.

The experimentally determined properties are summarized in table 4.4.

Table 4.4. Curie temperature, saturation magnetization and coercive field ($\mu_0 H_C$) for x ranging from 0 to 0.4. The coercive field was determined from the hysteresis loops from figure 4.12.

x	T_C (K)	M_S (μ_B/f.u.)	$\mu_0 H_C$ (T)
0	647	6.39	0.05
0.1	605	5.99	0.41
0.2	565	6.06	0.72
0.3	573	5.56	0.66
0.4	565	5.42	0.66

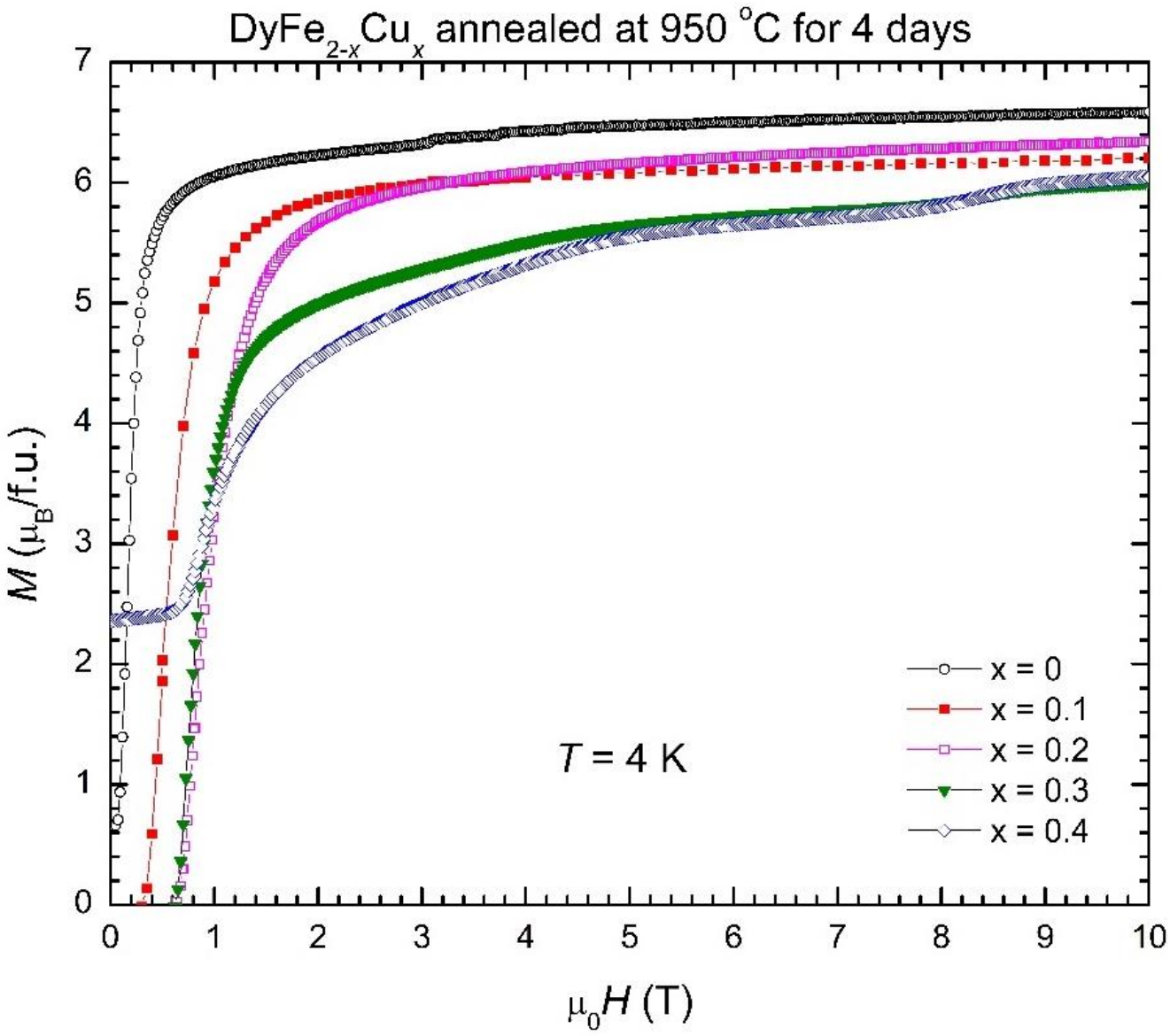

Figure 4.10. Magnetization isotherms at 4 K.

The Curie temperature has a significant decrease from 647 K in the $DyFe_2$ intermetallic compound to 565 K at a Cu concentration $x = 0.2$ in the doped $DyFe_{2-x}Cu_x$ compounds. However, for higher values of x there is no further decrease and a plateau is reached. This behaviour can be explained in the context of the main interactions that occur in these types of systems. The strongest interaction is between the 3d electron shells of the transition metals ($M - M$ interaction). The Curie temperature will be mainly determined by the magnitude of this interaction, which depends on the distance between the atoms and the number of nearest neighbours. Although the addition of Cu does not significantly alter the nearest neighbour distance between the Fe atoms, the number of magnetic nearest neighbours decreases. Therefore, the decrease in the Curie temperature is a result of magnetic dilution. The plateau reached at $x = 0.2$ suggests that a solubility limit of the Cu in the $DyFe_2$ phase is reached.

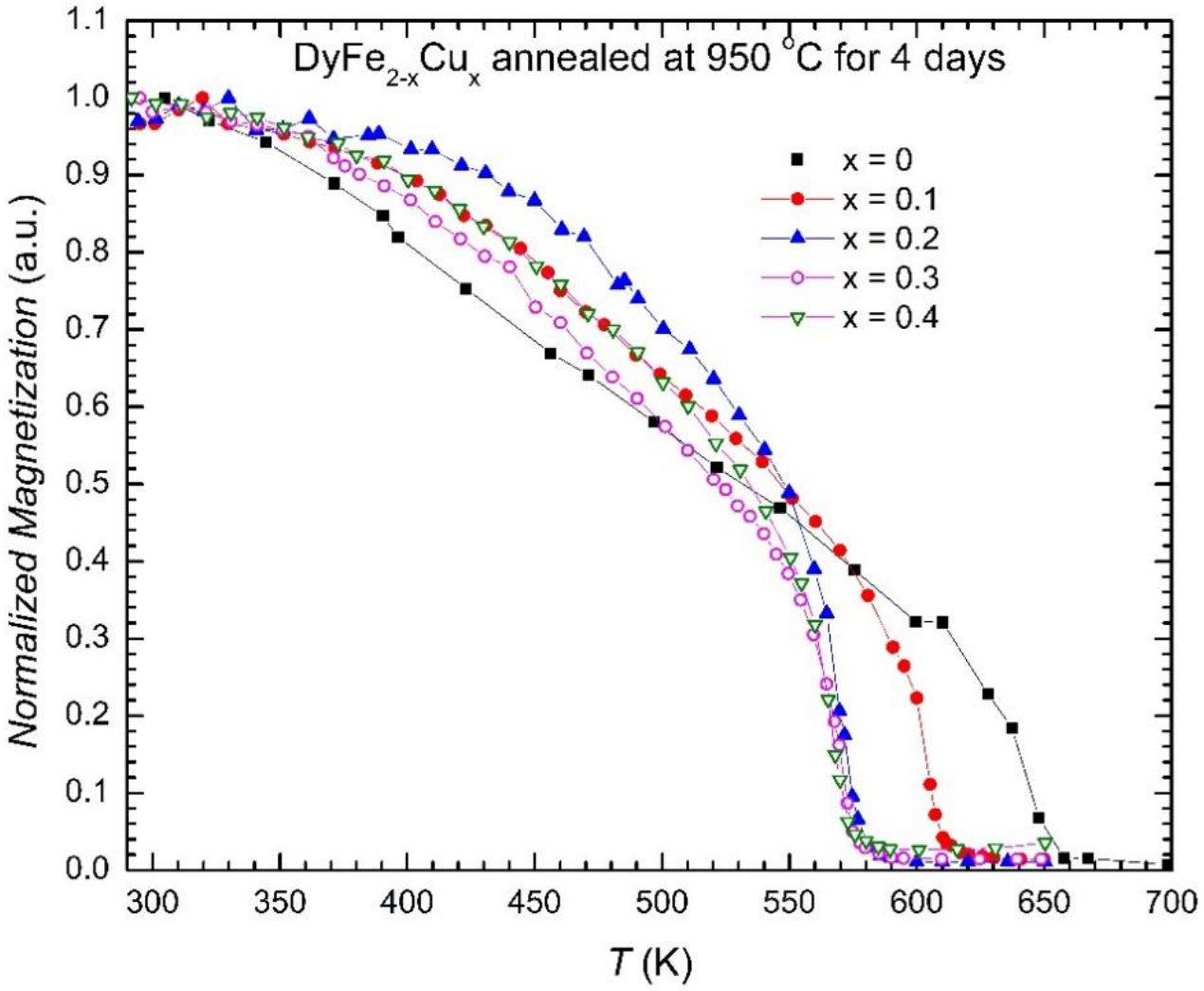

Figure 4.11. Normalized magnetization as a function of temperature.

Given the increase in the total magnetic moment indicated by the computational results, the saturation magnetization is expected to increase with the Cu concentration. However, the experimental results show an opposite behaviour. This could be due to a possible canting of the magnetic moments when adding Cu. The Dy and Fe moments are no longer antiparallel, but at an angle different from 180 degrees, which alters the ferrimagnetic ordering of the compound.

The significant increase in the coercive field from $x = 0$ to $x = 0.2$ can be attributed to a possible enhancement of the magnetocrystalline anisotropy related to the addition of Cu. This could also account for the metamagnetic transition that can be observed for $x \geq 0.3$ around the 8 T field value – figure 4.10. As in the case of the Curie temperature, a plateau for the coercive field is reached at $x = 0.2$, which also supports the solubility limit hypothesis. This can be further explained by taking into account the XRD patterns, which show that the $DyFe_3$ phase becomes

dominant with the increase of the Cu concentration. Therefore, the plateaus reached in the coercive field and in the Curie temperature can be explained by Cu going preferentially into the $DyFe_3$ impurity phase above the solubility limit.

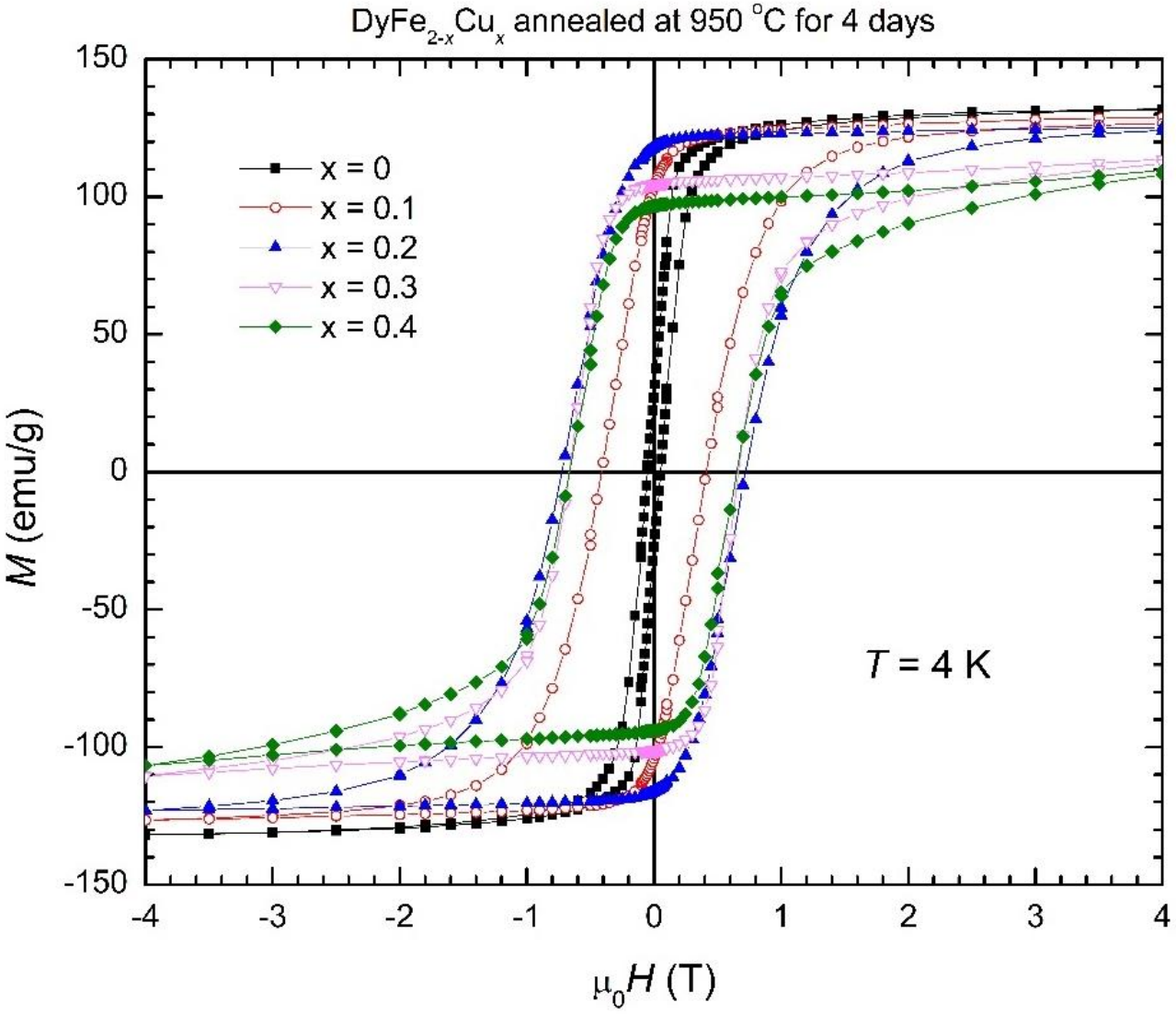

Figure 4.12. M(H) (hysteresis) loop at 4K.

Conclusions

The structural and magnetic properties of the $DyFe_{2-x}Cu_x$ intermetallic compounds were investigated by both computational and experimental means. For the experimental part, the samples were prepared under arc-melting and then annealed at 950 °C for 4 days.

The XRD characterization of the as-cast samples showed a phase mixture between the $DyFe_2$ and $DyFe_3$ phases. The diffraction patterns of the annealed samples showed that for the $0 \leq x \leq 0.4$ copper concentration range, the samples presented a majority $DyFe_2$ type phase, in the $0.5 \leq x < 1$ there is a phase mixture of $DyFe_2$ and $DyFe_3$ and for $x \geq 1$, the $DyFe_3$ phase becomes dominant. The XRD patterns confirmed that the annealing process improved the crystallinity and homogeneity of the sample.

The computational results showed that the lattice parameter of the compounds has a low variation with respect to the addition of copper, an expected result, also confirmed by the XRD determined structural information. The magnetic moment increased with the addition of copper, due to magnetic dilution and the decrease in the Fe magnetic moments. However, the results may not be quantitatively accurate, due to the limitation of the methods and the software used, which disregard the spin-orbit coupling, leading to an underestimated Dy atomic magnetic moment.

The VSM and Weiss balance measurements provided the Curie temperature, saturation magnetization and coercive field of the compounds. The Curie temperature decreased from 647 K for $x = 0$ to 565 K for $x = 0.2$, reaching a plateau at this Cu concentration. This behaviour is attributed to a decrease in the number of nearest magnetic neighbours with the increase of the Cu concentration. The saturation magnetization decreased from 6.39 μ_B/f.u. for $x = 0$ to 5.42 μ_B/f.u for $x = 0.4$ due to a possible canting of the magnetic moments with the addition of Cu. The coercive field increased from 0.05 T at $x = 0$ to 0.72 T at $x = 0.2$, reaching a plateau. The increase in the coercive field can be attributed to an enhancement of the magnetocrystalline anisotropy when adding Cu. The plateau reached around the $x = 0.2$ in both the Curie temperature and coercive field may be explained through a solubility limit at this concentration, above which Cu crystallizes in the $DyFe_3$ phase.

Further potential improvements include the addition of spin-orbit coupling in the computational method and the refining of the annealing process, to obtain single phase $DyFe_2$ type compounds for the copper concentration $x \geq 0.5$.

References

[1] Introduction to Solid State Physics, Eighth Edition, Charles Kittel, 1953.

[2] N. W. Ashcroft, N. D Mermin, Solid State Physics, Harcourt College Publishers, Fort Worth, Philadelphia, San Diego, 1976.

[3] Fundamentals of Powder Diffraction and Structural Characterization of Materials, Second Edition, Vitalij K. Pecharsky, Peter Y. Zavalij, Springer New York, NY, 2009.

[4] R. M. Martin, Electronic Structure: Basic Theory and Practical Methods, Cambridge University Press, New York, 2004.

[5] Magnetism and Magnetic Materials, J.M.D. Coey, 2009.

[6] V. Pop, I. Chicinaş, N. Jumate, Fizica Materialelor. Metode experimentale, Presa Universitară Clujeană, Cluj-Napoca, 2001.

[7] S. Mican, Magnetic Properties of 3d Transition Metals in Intermetallic Compounds and Oxides, Teză de Doctorat, Universitatea Babeş-Bolyai, Cluj-Napoca, 2012.

[8] A. Tishin, Y. Spichkin, The Magnetocaloric Effect and its Applications, Institute of Physics Publishing, Bristol and Philadelphia, 2003.

[9] Burrola Gándara, L.A.; Vázquez Zubiate, L.; Carrillo Flores, D.M.; Elizalde Galindo, J.T.; Ornelas, C.; Ramos, M. Tuning Magnetic Entropy Change and Relative Cooling Power in $La_{0.7}Ca_{0.23}Sr_{0.07}MnO_3$ Electrospun Nanofibers. Nanomaterials 2020, 10, 435.

[10] K. Buschow, Intermetallic compounds of rare-earth and 3d transition metals, Rep. Prog.Phys , 40, 1179-1256, 1977.

[11] Momma, K. & Izumi, F. (2011). J. Appl. Cryst. 44, 1272-1276.

[12] M. Mansmann and W. E. Wallace , "Magnetic Properties of $GdFe_2$ and $DyFe_2$", J. Chem. Phys. 40, 1167-1168 (1964).

[13] H. Oesterreicher and Roland Pitts , "Structural and magnetic studies on $DyFe_2$–$DyAl_2$ and $DyCo_2$–$DyAl_2$", Journal of Applied Physics 43, 5174-5179 (1972).

[14] Susanne Landin, John Ågren, Thermodynamic assessment of Fe-Tb and Fe-Dy phase diagrams and prediction of Fe-Tb-Dy phase diagram, Journal of Alloys and Compounds, Volumes 207–208, 1994, Pages 449-453.

[15] A. Clark, R. Abbundi and W. Gillmor, "Magnetization and magnetic anisotropy of TbFe2, DyFe2, Tb0.27Dy0.73Fe2and TmFe2," in IEEE Transactions on Magnetics, vol. 14, no. 5, pp. 542-544, September 1978, doi: 10.1109/TMAG.1978.1059879.

[16] Laboratory preparation of intermetallic phases, R. Ferro, A. Saccone, Pergamon Materials Series, Pergamon, Volume 13, 2008, Pages 531-616.

[17] Introduction to Magnetic Materials, Second Edition, B. D. Cullity, C. D. Graham, 2014.

[18] P. Hohenberg, W. Kohn, Inhomogeneous electron gas, Phys. Rev., 136, 3B, 864-871, 1964.

[19] Self-Consistent Equations Including Exchange and Correlation Effects, W. Kohn and L. J. Sham, Phys. Rev. 140, A1133, 15 November 1965.

[20] V. I. Anisimov, First-principles calculations of the electronic structure and spectra of strongly correlated systems: the LDA+U method, J. Phys.: Condens. Matter, 9, 4, 767-808 1997.

[21] https://www.abinit.org/ 16/06/2022.

[22] M. Torrent, F. Jollet, F. Bottin, G. Zerah, and X. Gonze, "Implementation of the Projector Augmented-Wave Method in the ABINIT code.", Comput. Mat. Science 42, 337, (2008).

[23] J. P. Perdew, K. Burke, M. Ernzerhof, Phys. Rev. Lett., 77 (1996) 3865–3868.

[24] M. A. Marques, M. J. Oliveira, T. Burnus, Comput. Phys. Commun., 183 (10) (2012) 2272–2281.

[25] Niggli reduction and Bravais lattice determination, H. L. Shi and Z. A. Li, J. Appl. Cryst. (2022). 55, 204-210.

[26] François Jollet, Marc Torrent, Natalie Holzwarth, Generation of Projector Augmented-Wave atomic data: A 71 element validated table in the XML format, Computer Physics Communications, Volume 185, Issue 4, 2014, Pages 1246-1254.

[27] Standard model of the rare earths analyzed from the Hubbard I approximation, I. L. M. Locht, Y. O. Kvashnin, D. C. M. Rodrigues, M. Pereiro, A. Bergman, L. Bergqvist, A. I. Lichtenstein, M. I. Katsnelson, A. Delin, A. B. Klautau, B. Johansson, I. Di Marco, and O. Eriksson, Phys. Rev. B 94, 085137 – Published 22 August 2016

[28] E. T. Teatum, K. A. Gschneidner, Jr., J. T. Waber, Compilation of calculated data useful in predicting metallurgical behavior of the elements in binary alloy systems., Tech. Rep. LA-4003, Los Alamos Scientific Laboratory of the University of California, Los Alamos, New Mexico (December 1968).

[29] Norgren, S., Hodaj, F., Colinet, C. et al. Experimental investigation on the enthalpies of formation of the $DyFe_2$, $DyFe_3$, Dy_2Fe_{17}, $ErFe_2$, and $ErFe_3$ intermetallic compounds. Metall Mater Trans A 29, 1367–1374 (1998).

DECLARAȚIE PE PROPRIE RĂSPUNDERE

Subsemnatul, Radu-George Hațegan, declar că Lucrarea de disertație intitulată “Structural and Magnetic Properties of $DyFe_{2-x}Cu_x$ Intermetallic Compounds” pe care o voi prezenta în cadrul examenului de finalizare a studiilor la Facultatea de Fizică, din cadrul Universității Babeș-Bolyai, în sesiunea iunie 2022, sub îndrumarea Lect. Dr. Ing. Sever Mican, reprezintă o operă personală. Menționez că nu am plagiat o altă lucrare publicată, prezentată public sau un fișier postat pe Internet. Pentru realizarea lucrării am folosit exclusiv bibliografia prezentată și nu am ascuns nici o altă sursă bibliografică sau fișier electronic pe care să le fi folosit la redactarea lucrării.

Prezenta declarație este parte a lucrării și se anexează la aceasta.

Data,
21.06.2022

Radu-George Hațegan,

Semnătură